

GALACTIC OUTFLOWS AND PHOTOIONIZATION HEATING IN THE REIONIZATION EPOCH

K. FINLATOR^{1,2}

University of California Santa Barbara, Santa Barbara, CA 93106

R. DAVÉ AND F. ÖZEL

University of Arizona, Department of Astronomy, Tucson, AZ 85721

Draft version October 14, 2011

ABSTRACT

We carry out a new suite of cosmological radiation hydrodynamic simulations that explores the relative impacts on reionization-epoch star formation of galactic outflows and photoionization heating from a self-consistently grown extragalactic ultraviolet ionizing background (EUVB). We compare the predictions with observational constraints from the cosmic microwave background, the ultraviolet continuum luminosity function of galaxies, and the Lyman- α forest. By itself, an EUVB suppresses the luminosity function by less than 50% at $z = 6$ even if it is orders of magnitude stronger than observed. This overproduces the observed galaxy abundance by a factor of 3–5, indicating the need for an additional feedback process. We confirm that outflows readily suppress both the EUVB and the luminosity function into improved agreement with observations. Population I–II star formation can reionize the Universe by $z = 6$ even in the presence of strong feedback from photoheating and outflows. The resulting EUVB suppresses star formation in halos with virial temperatures below 10^5 K but has a weaker impact in more massive halos. Nonetheless, halos with virial temperatures below 10^5 K contribute up to $\sim 50\%$ of all ionizing photons owing to the EUVB’s inhomogeneity. Overall, star formation rate scales with halo mass M_h as $M_h^{1.3-1.4}$ for halos with $M_h = 10^{8.2-10.2} M_\odot$. This is a steeper dependence than is often assumed in reionization models, boosting the expected power spectrum of 21 centimeter fluctuations on large scales. The luminosity function rises steeply to at least $M_{1600} = -13$ even in models that treat both outflows and an EUVB, indicating that reionization was driven by faint galaxies ($M_{1600} \geq -15$) that have not yet been observed. Outflows and an EUVB interfere with each other’s feedback effects in two ways: Outflows weaken the EUVB, limiting Jeans suppression of low-mass halos; this leads to overall de-amplification of suppression at early times ($z > 8$). Meanwhile, they amplify each other’s impact on more massive halos, leading to overall amplification of suppression at later times. Our models cannot simultaneously explain observations of galaxies, the cosmic microwave background, and the intergalactic medium. Correcting for dynamic range limitations and adjusting our physical treatments will alleviate discrepancies, but observations may still require additional physical scalings such as a mass-dependent ionizing escape fraction.

Subject headings: radiative transfer — galaxies: evolution — galaxies: high-redshift — galaxies: photometry — galaxies: star formation — dark ages, reionization, first stars

1. INTRODUCTION

Understanding the processes that governed galaxy growth when the Universe was less than one billion years old represents a central challenge for the upcoming decade. On the largest scales, the feedback effect of galaxies on the temperature, ionization state, and enrichment of the intergalactic medium (IGM) will be probed through absorption by neutral hydrogen (Fan et al. 2006) and metals (Oh 2002; Oppenheimer et al. 2009); through its imprint on the cosmic microwave background (Komatsu et al. 2011); and through redshifted emission by neutral hydrogen (Furlanetto et al. 2006). On much smaller scales, observations of the Milky Way and its environment will decode the signature left by reionization in low-mass objects (Bullock et al. 2000). Between these two regimes, direct observations will constrain the formation of the first quasars, gamma-ray bursts, and galaxies.

With the realization that quasars could not have reionized the Universe by themselves (Madau et al. 1999; Dijkstra et al. 2004b; Willott et al. 2010; Treister et al. 2011), much attention is now focused on understanding the galaxies. Using sensitive measurements from the Wide Field Camera 3 aboard the Hubble Space Telescope (HST), the Infrared Array Camera (IRAC) aboard the Spitzer Space Telescope, and other facilities, a number of groups have begun to constrain the abundance and colors of continuum-selected galaxies out to $z \sim 10$ (for example, Finkelstein et al. 2010; Bouwens et al. 2011b; Dunlop et al. 2011; González et al. 2011; Grazian et al. 2011; McLure et al. 2011; Oesch et al. 2011). In a complementary approach, several groups have identified tens to hundreds of galaxies at $z \geq 6$ through their bright Lyman- α emission lines. These catalogs have already begun to constrain the luminosity function, star formation, and clustering properties of faint galaxies (Hu et al. 2010; Ouchi et al. 2010; Tilvi et al. 2010; Kashikawa et al. 2011). The James Webb Space Telescope (JWST) will soon push the observational frontier

¹ Hubble Fellow

² finlator@physics.ucsb.edu

back to even earlier times (Gardner et al. 2009).

Interpreting these measurements as constraints on the feedback processes that regulated early star formation requires insight from theoretical models. To date, models have demonstrated that star formation in low-mass halos is influenced by at least two feedback processes, namely galactic outflows from star-forming regions and photoionization heating (hereafter, photoheating) owing to an extragalactic ultraviolet background (EUVB). Strong galactic outflows are expected in low-mass systems (Dekel & Silk 1986) but have in fact been observed in star-forming galaxies up to the highest masses (Weiner et al. 2009). Cosmological hydrodynamic simulations have shown that they are required in order to reconcile simulations with post-reionization observations of galaxy abundances (Davé et al. 2006) and scaling relations (Davé et al. 2006; Finlator & Davé 2008; Davé et al. 2011a,b) as well as the enrichment of the IGM (Oppenheimer & Davé 2006, 2008).

Photoheating impacts star formation by depleting the baryon fractions in low-mass halos (Shapiro et al. 1994; Thoul & Weinberg 1996; Gnedin 2000; Dijkstra et al. 2004a; Okamoto et al. 2008). In fact, the impact of an EUVB is often used to divide halos into three categories (for example, Haiman 2009): Halos with virial temperatures in the range $300 \lesssim T_{\text{vir}} \lesssim 10^4 \text{K}$ can use molecular hydrogen to cool their gas to star-formation densities, but they are susceptible to feedback from a background in the H_2 -dissociating Lyman-Werner bands. Halos with $10^4 \lesssim T_{\text{vir}} \lesssim 10^5 \text{K}$ can cool their gas through collisional excitation of neutral hydrogen, but only in the absence of a Lyman continuum background. More massive halos can grow galaxies even in the presence of an EUVB. For the purposes of this paper, we shall refer to halos with $T_{\text{vir}} \leq 10^4 \text{K}$ (virial velocities of $\leq 20 \text{ km s}^{-1}$) as “minihalos”; halos with $T_{\text{vir}} = 10^{4-5} \text{K}$ ($20\text{--}64 \text{ km s}^{-1}$) as “photosensitive”, and more massive halos as “photoreistant”.

High-resolution radiation hydrodynamic simulations now indicate that a single supernova can unbind a minihalo’s entire gas reservoir (Kitayama & Yoshida 2005; Greif et al. 2007; Wise & Abel 2008b). The contribution of minihalos to cosmological reionization is therefore probably weak, although their contribution to the metal enrichment of star-forming gas may be important (Wise & Abel 2008a). Photoreistant halos are simpler to model because they respond weakly to an EUVB. This means that the largest uncertainty in our understanding of reionization involves the amount of star formation in the abundant but fragile photosensitive halos. If the inhomogeneous EUVB does not reach a significant fraction of photosensitive halos until late times, then they could have dominated the star formation density (Barkana & Loeb 2000) and hence the ionizing photon emissivity (Choudhury & Ferrara 2007; Muñoz & Loeb 2011) throughout much of the reionization epoch.

The efficiency of feedback in photosensitive halos is also important because of its indirect impact on the more massive halos into which they merge. In particular, feedback influences not only the lowest-mass system that is permitted to form stars, but also the way in which the star formation rate (SFR) scales with the halo mass (M_h)

at higher masses. This hierarchical filtering is not accounted for in idealized models (Thoul & Weinberg 1996; Dijkstra et al. 2004a), but it is important because the resulting SFR- M_h scaling, when modulated by the dependence of the ionizing escape fraction f_{esc} , determines the expected power spectrum of 21-centimeter fluctuations at a given ionization state (McQuinn et al. 2007).

As such, it is a key ingredient in numerical simulations of reionization. Over the past decade, a number of groups have used simple models for star formation in dark matter halos to model the reionization of representative cosmological volumes (Sokasian et al. 2003; Gnedin & Fan 2006; Kohler et al. 2007; Trac & Cen 2007; Trac et al. 2008; Iliev et al. 2007; Aubert & Teyssier 2010; see also the review in Trac & Gnedin 2009). These groups have achieved impressive success in relating the growth of structure across a wide dynamic range to observational constraints on reionization from the cosmic microwave background (CMB) and the Lyman- α forest. However, their predictions remain dependent on the assumed conversion from M_h to SFR (McQuinn et al. 2007), and few of them have confronted post-reionization observations that constrain this scaling such as the IGM temperature or the galaxy LF (see, however, Zheng et al. 2010 and Petkova & Springel 2010).

Ideally, models that use galaxies to reionize the Universe should be tested against observations of galaxies. For the foreseeable future, the two principal constraints on star-forming galaxies will be the Lyman- α luminosity function (LF) of Lyman- α emitters (LAEs) and the ultraviolet (1350-1600 Å) continuum LF of Lyman-break galaxies (LBGs). Efforts to date have focused more on modeling the LAE LF because its observed evolution should be sensitive to the late stages of reionization (Malhotra & Rhoads 2006; McQuinn et al. 2007; Iliev et al. 2008). Unfortunately, this exercise depends on assumptions regarding both the star formation efficiency within halos of different masses and the escape fraction of Lyman- α photons (Zheng et al. 2010). Estimating the contribution of LAEs to reionization depends additionally on the unknown escape fraction of ionizing photons. In short, it is easier to model the impact of incomplete reionization on an assumed intrinsic LAE LF than to constrain star formation based on the observed one.

Using the ultraviolet continuum LF (hereafter, the LF) to constrain the galaxy contribution to reionization has to date been prevented by two concerns. First, the LF is an uncertain tracer of star formation owing to the unknown amount of dust extinction. Recent work has demonstrated that galaxies at $z = 6$ have quite blue UV continua, suggesting that they are relatively dust-free (Bouwens et al. 2010a; Finkelstein et al. 2010; Dunlop et al. 2011). If true, then inferring SFRs of LBGs from their 1350–1600 Å luminosities is less uncertain at $z \geq 6$ than at lower redshifts. The uncertainty in the ionizing emissivity of galaxies then reduces to a single parameter, the ionizing escape fraction. This parameter remains uncertain, but observations now suggest that it was larger at early times than at present (Siana et al. 2010), and may have been as high as 50% (Rauch et al. 2011). The second obstacle was the small available sample sizes at $z \geq 6$. Recently, however,

observations have begun to constrain the reionization-epoch LF (McLure et al. 2011; Bouwens et al. 2011a). There is now a broad consensus as to the abundance of bright galaxies at $z = 7$ (McLure et al. 2011); constraints at $z = 8$ have emerged; and star-forming galaxy candidates have even been identified at $z = 10$ (Stark et al. 2007; Bouwens et al. 2011a; Oesch et al. 2011). These observations are currently being reinforced by even more complete samples from the Cosmic Assembly Near-Infrared Deep Extragalactic Legacy Survey (CANDELS; Grogin et al. 2011, Koekemoer et al. 2011). They do not yet directly constrain star formation in photosensitive halos, whose galaxies remain fainter than current detection limits. However, the blue observed UV continua indicate that they constrain the star formation within photoresistant halos fairly directly, which may be invoked as an indirect constraint at fainter luminosities.

Progress in understanding the significance of photosensitive halos requires a model for galaxy evolution that can be tested against the extensive observational constraints from the post-reionization Universe, and that can be extrapolated into the reionization epoch through the incorporation of a self-consistently grown inhomogeneous EUVB. Such a model would treat not only the spatial inhomogeneity of photoheating, but also the nonlinear couplings between different feedback processes (Pieri & Martel 2007; Pawlik & Schaye 2009).

Cosmological hydrodynamic simulations represent a mature theoretical model for galaxy evolution that can serve as a starting point. Over the last decade, numerous studies have shown that the adoption of theoretically- and empirically-motivated models for galactic outflows brings their predictions into reasonable agreement with a wide variety of observations of the IGM (Oppenheimer & Davé 2006, 2008) and of galaxies (Davé et al. 2006; Finlator & Davé 2008; Finlator et al. 2011; Davé et al. 2011a,b). These studies have generally assumed a spatially-uniform, optically thin EUVB such as that of Haardt & Madau (2001, hereafter HM01). In order to adapt this framework for the reionization epoch, we recently developed a time-dependent continuum radiative transfer technique that is optimized for cosmological volumes (Finlator et al. 2009a). We used this method to model the growth of ionized regions on snapshots extracted from existing simulations and verified that outflows leave enough star formation to reionize the IGM by $z = 6$ (Finlator et al. 2009b). We have since integrated this method into our custom version of GADGET-2, enabling us to extend our previous work into the reionization epoch with improved realism.

In this study, we use this machinery to take a step toward the assembly of a complete understanding of how star formation may have powered reionization by modeling the relative roles of photoheating and outflows within the context of three dimensional radiation hydrodynamics simulations that successfully complete reionization by $z = 6$. We will consider simulations with and without each of these feedback processes, for a total of four kinds of simulations. This will allow us to explore how strong each process is separately as well as how they interact when treated simultaneously.

In § 2, we discuss our custom version of GADGET-2, our radiation transport solver and our approach to mea-

suring galaxy and halo properties from simulation snapshots. In § 3, we explore how an EUVB and galactic outflows impact the baryon mass fractions and star formation rates of halos, both separately and when considered together. We then integrate over all halos in order to show how they impact the volume-averaged ionizing emissivity and star formation rate density (SFRD). In § 4, we map these predictions into observable space by exploring the normalization and shape of the predicted galaxy LF. In § 5, we discuss our simulated reionization histories and compare with inferences from the cosmic microwave background and the Lyman- α forest. Finally, we summarize our results in § 6. We use a standard test case to evaluate our code in an appendix.

2. COSMOLOGICAL RADIATIVE HYDRODYNAMIC SIMULATIONS WITH GADGET-2

In this Section, we describe our numerical methods. Briefly, we run a suite of cosmological radiation hydrodynamic simulations that use our custom version of GADGET-2 to treat gravity and gas dynamics and are coupled with our custom radiation transport solver. We identify galaxies in post-processing using SKID and dark matter halos using FOF. Finally, we compute the galaxies' broadband photometric colors by convolving their star formation histories and metallicities with the Bruzual & Charlot (2003) stellar population synthesis models. We use a tophat filter of width 100 Å centered at 1600 Å to define the UV continuum luminosity.

2.1. Hydrodynamics, Star Formation and Outflows

We model structure formation using our custom version of the parallel cosmological galaxy formation code GADGET-2 (Springel 2005). This code implements a formulation of smoothed particle hydrodynamics (SPH) that simultaneously conserves entropy and energy and solves for the gravitational potential with a tree-particle-mesh algorithm.

Gas particles undergo radiative cooling using the processes and rates in Table 1 of Katz et al. (1996). We account for metal-line cooling using the collisional ionization equilibrium tables of Sutherland & Dopita (1993). The cooling rate depends on the ionization state, hence cooling and ionizations must be computed together. We achieve this using a nested subcycling approach that we describe below. We initialize the IGM temperature and neutral hydrogen fraction to the values appropriate for each simulation's initial redshift as computed by RECFast (Wong et al. 2008; see §2.4), and we assume that helium is initially completely neutral.

As gas particles cool, they acquire a subgrid two-phase interstellar medium consisting of hot gas that condenses via a thermal instability into cold star-forming clouds, which are in turn evaporated back into the hot phase by supernovae (McKee & Ostriker 1977). They also acquire the ability to stochastically spawn star particles via a Monte Carlo algorithm. This treatment requires only one physical parameter, the star formation timescale, which is tuned to reproduce the Kennicutt (1998) relation (Springel & Hernquist 2003). The physical density threshold for star formation is 0.13 cm^{-3} . We account for metal enrichment owing to supernovae of Types II and Ia as well as asymptotic giant branch

stars; see Oppenheimer & Davé (2008) for details of the implementation.

We model galactic outflows (hereafter, “outflows”) using a Monte Carlo algorithm that applies kicks to star-forming SPH particles. We tune the probability that particles are kicked and the kick velocity such that the resulting outflow mass loading factor and wind speeds follow the scalings expected for momentum-driven winds (Murray et al. 2005). In this model, the ratio of the rate at which material enters the outflow to the SFR η_W varies with the host halo velocity dispersion σ as $\eta_W = \sigma_0/\sigma$ where the outflow amplitude $\sigma_0 = 150 \text{ km s}^{-1}$ is a free parameter and σ is estimated during the simulation using an on-the-fly group finder. The outflow velocity is proportional to σ . This model broadly reproduces observations of metals in the high-redshift IGM (Oppenheimer & Davé 2008; Oppenheimer et al. 2010).

2.2. Photoionization Feedback

2.2.1. Discretization

Our radiative transport (RT) solver discretizes the radiation field on a three-dimensional Cartesian grid and is hence Eulerian. By contrast, GADGET-2 discretizes the fluid equations using Smoothed Particle Hydrodynamics (SPH) and is hence Lagrangian. We now describe how we translate between these two discretizations.

The conversion from the SPH field to the RT grid occurs when we compute the emissivity field owing to star-forming regions and the opacity field owing to partially ionized and neutral gas. The volume-weighted mean emissivity η in an RT cell is given by an integral over the cell’s volume V :

$$\eta = \frac{1}{V} \int_V \eta(\mathbf{r}) d\mathbf{r}. \quad (1)$$

We derive $\eta(\mathbf{r})$ from the SFRs of star-forming gas particles. We account for the metallicity dependence of each particle’s emissivity using the following fitting function:

$$\log(Q) = 0.639(-\log(Z))^{1/3} + 52.62 - 0.182 \quad (2)$$

Here, Q is in $s^{-1}(\text{M}_\odot \text{yr}^{-1})^{-1}$, Z is the metal mass fraction, and the last term converts to a Chabrier (2003) initial mass function (IMF). This function reproduces the equilibrium emissivities of Schaerer (2003, Table 4) to 15% throughout the range $Z \in [10^{-7}, 0.04]$. We do not extrapolate this fit to metallicities outside this range.³

Owing to the fact that gas particles are spatially extended and generally straddle cell boundaries, Equation 1 becomes, for each cell, a sum over the SPH kernel-weighted volume means owing to the SPH particles that overlap that cell:

$$\eta = \sum_i \int_V W(\mathbf{r}_i - \mathbf{r}, h_i) \eta_i dV \quad (3)$$

Here, η_i is the emissivity of particle i , \mathbf{r}_i is the particle’s position, h_i is its smoothing length, and W is the SPH

³ We have verified that doing so has negligible impact on our results, which suggests that the ionizing emissivity boost from hypothetical zero-metallicity stars in atomically-cooled halos has negligible impact on cosmological scales.

smoothing kernel. We evaluate equation 3 by fitting a Gaussian to each SPH particle’s smoothing kernel so that its contribution to each of its neighboring cells reduces to a sum over incomplete gamma functions.

Equations 1–3 yield the total ionizing photon production rate within a cell, but only a fraction f_{esc} of these escape into the IGM. We do not have the spatial resolution to model f_{esc} self-consistently, hence we treat it as a free parameter and set it to a uniform value of 50% for all halos. We will show in Figure 12 that this choice leads to reionization completing by $z \approx (7, 6)$ in our fiducial simulation volume (without, with) outflows.

In our previous calculations, we found that a much lower fiducial value of $f_{\text{esc}} = 0.12$ led to reionization completing by $z = 6$ (Finlator et al. 2009b). Two differences lead to the higher value that we adopt here. First, our post-processing simulations did not account for subgrid gas clumping, hence they underestimated the recombination rate. In our current simulations, recombinations and cooling are computed directly on the SPH particles, automatically capturing gas clumping that occurs on scales smaller than the radiative transfer grid cells. Second, the simulations on which we previously post-processed radiative transport calculations assumed the HM01 EUVB. This background assumes a significant contribution from quasars and is harder than our self-consistently derived galaxies-only background. The resulting density field, which was an input into our post-processing radiation transport calculations, possessed a higher temperature, significantly more Jeans smoothing, and a lower recombination rate than occurs in our newer, self-consistent calculations. Tuning our simulations to achieve reionization by $z = 6$ given our softer background therefore requires a higher f_{esc} .

Each RT cell’s opacity χ is also given by a volume-weighted mean:

$$\chi = \frac{1}{V} \int_V \chi(\mathbf{r}) dV. \quad (4)$$

This equation is identical to Equation 1 except that the emissivity has been replaced with the opacity, hence we evaluate it in the same way. The opacity $\chi(\mathbf{r})$ is the neutral hydrogen abundance multiplied by the absorption cross section $\sigma_{\text{HI}} = 6.30 \times 10^{-18} \text{ cm}^2$. We neglect the opacity owing to star-forming gas particles because their absorptions are implicitly taken into account through f_{esc} . Adopting a smaller cross section in order to match the mean energy of ionizing photons (see below) would yield a more diffusive EUVB without qualitatively changing our results.

The translation from the RT grid back to the SPH field occurs when we compute the photoionization and photoheating rates. This involves, for each SPH particle, summing the contributions owing to the radiation fields from each of its neighboring cells. For example, the photoionization rate Γ_i for SPH particle i is given by the integral (over all space)

$$\Gamma_i = \int W(\mathbf{r}_i - \mathbf{r}, h_i) \Gamma(\mathbf{r}) dV, \quad (5)$$

where $\Gamma(\mathbf{r})$ is the gridded photoionization rate. We evaluate Equation 5 by fitting a Gaussian to each particle’s smoothing kernel, which again reduces the integral to a

sum over incomplete gamma functions.

The photoheating rate owing to the photoionization of hydrogen ϵ_{HI} is the hydrogen photoionization rate Γ_{HI} times the latent heat per photoionization ϵ_{HI}

$$\epsilon_{\text{HI}} = \frac{\int 4\pi\sigma_{\nu}J_{\nu}\frac{h(\nu-\nu_{\text{LL}})}{h\nu}d\nu}{\int 4\pi\sigma_{\nu}J_{\nu}\frac{1}{h\nu}d\nu}, \quad (6)$$

where J_{ν} is the mean specific intensity and the integrals run from the Lyman Limit ν_{LL} to ∞ . ϵ_{HI} depends on many factors including the intrinsic slope of the ionizing continuum and the impact of spectral hardening in the ISM and the IGM (e.g., Tittley & Meiksin 2007). If the simulation volume is large compared to the photon mean free path, then all photons are absorbed and we may drop the frequency-dependent cross sections σ_{ν} from equation 6 to obtain a volume-averaged ϵ_{HI} . The EUVB may be approximated as a power law $J_{\nu} \propto \nu^{-\alpha}$ such that ϵ_{HI} depends only on the slope α . α can vary between 5 for Population I stars and 1.8 for quasars, leading to values for ϵ_{HI} in the range 0.25–0.64 Ryd. By applying population synthesis models to the young, metal-poor galaxies that dominate our EUVB (§ 2.3), we find that their Lyman continua are characterized by $\alpha = 4$ –5 (see also Barkana & Loeb 2001). This corresponds to $\epsilon_{\text{HI}} = 0.25$ –0.32 Ryd. We adopt $\epsilon_{\text{HI}} = 0.3$ Ryd, or 4.08 eV of thermal heating per ionization. This value agrees well with the heating rate per ionization in the galaxies-only EUVB derived by HM01, but it is lower than the value of 0.6 Ryd assumed by Furlanetto & Oh (2009) or the range 0.47–2.2 Ryd considered by Petkova & Springel (2010). We have not varied ϵ_{HI} because it is chosen for consistency with the simulation’s predicted stellar populations (see § 5.3 for a discussion).

2.2.2. Solving the Radiative Transport Equation

We solve for the transport of ionizing radiation using the moment method presented in Finlator et al. (2009a). This approach divides the problem into two parts, a moment equation update and a long characteristics calculation that updates the Eddington tensors. We review this technique here and describe our parallelization strategy.

The zeroth and first angle moments of the radiation transport equation in cosmological comoving coordinates are:

$$\frac{\partial \mathcal{J}}{\partial t} = -\frac{1}{a}\vec{\nabla}_c \cdot \vec{\mathcal{F}} + 4\pi\eta - c\chi\mathcal{J} \quad (7)$$

$$\frac{\partial \vec{\mathcal{F}}}{\partial t} = -\frac{c}{a}\vec{\nabla}_c \cdot (c\mathbf{f}\mathcal{J}) - c\chi\vec{\mathcal{F}} \quad (8)$$

$$\mathbf{f} \equiv \frac{\int \mathcal{N}\hat{n}\hat{n}d\Omega}{\int \mathcal{N}d\Omega}. \quad (9)$$

Equation 7 relates the angle-averaged photon number density \mathcal{J} to the divergence of the photon flux $\vec{\mathcal{F}}$, the angle-averaged photon emissivity η , and the opacity χ , where χ accounts for attenuation owing to cosmological expansion, redshifting, and absorptions. In our simulations, η depends on the local stellar population and χ is dominated by the opacity of neutral hydrogen. Equation 8 relates the evolving photon flux to the divergence of the radiation pressure tensor (the quantity in the parentheses) and χ . We close the moment hierarchy

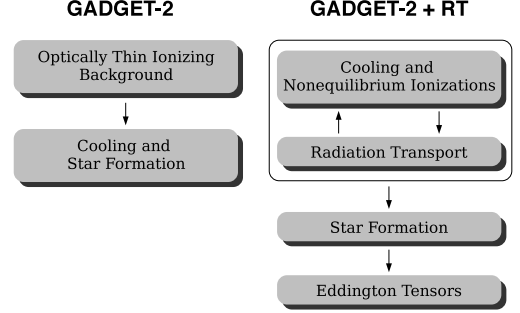


FIG. 1.— Flowcharts illustrating how the conventional flow of a single timestep in GADGET-2 (left) compares with our radiative hydrodynamic version (right).

by relating the radiation pressure tensor to \mathcal{J} using the Eddington tensor \mathbf{f} . We use Equation 9 to derive \mathbf{f} from the angle-dependent photon number density \mathcal{N} , which we in turn obtain from a time-independent ray-casting procedure (see §3 of Finlator et al. 2009a).

We discretize equations 7–8 fully implicitly in time in order to improve the code’s stability. We parallelize the solution to the resulting linear system of difference equations by decomposing the domain of radiative transfer grid cells over the set of compute nodes. We then iteratively solve the portion of the linear system that corresponds to each subdomain and then swap information at the subdomain boundaries. We obtain subdomain solutions from a single Gauss-Seidel iteration. This “Additive Schwarz Iteration” (Schwarz 1870) is straightforward to implement and lacks global synchronization points (because processors only need to swap information with processors that host neighboring subdomains).

The Eddington tensor \mathbf{f} encodes the angle dependence of the radiation field. Errors in the assumed \mathbf{f} lead to errors in the shapes of ionized regions (Figure 5 of Finlator et al. 2009a). In cases where the timescale over which the emissivity field changes is long compared to the simulation’s light-crossing time, obtaining \mathbf{f} from a time-independent calculation does not introduce large errors. The timescale for structure to form is roughly a Hubble time, hence this ratio is small for simulation volumes with comoving side length $\sim 10h^{-1}\text{Mpc}$ volumes at $z \sim 10$ (note that, throughout this work, we quote our simulation volumes’ sizes in comoving units). We compute \mathbf{f} as follows: After each timestep, we evaluate whether \mathcal{J} has changed within a cell by more than 5%. If so, then we update its Eddington tensor by casting rays to every source that is not obscured by an optical depth greater than 6. We mimic periodic boundaries using a single layer of periodic replica volumes. We parallelize this step by first gathering the updated opacity and emissivity fields onto all of the compute nodes and then assigning roughly equal numbers of updates to each compute node. Afterwards, we gather the updated Eddington tensors onto all of the compute nodes.

2.2.3. Merging the Radiation and Hydrodynamic Solvers

Figure 1 illustrates how the addition of our radiation transport solver modifies the flow of a single timestep in GADGET-2. In the case of a spatially-uniform, opti-

cally thin EUVB (left side), each timestep involves first updating the EUVB and then allowing the gas to cool and form stars. In the case of radiation hydrodynamic simulations (right side), we first update the radiation, ionization, and temperature fields simultaneously. This step involves three layers of nested loops. The outermost loop consists of an iteration between one module that advances the gas ionization and thermal state and a second module that advances the radiation field. Within the ionization/cooling module, an inner loop alternately advances the cooling equations explicitly and then the ionization equations implicitly using substeps that are limited to $0.002u/\dot{u}$, where u is the particle’s internal energy. The ionization solver is itself a Newton-Raphson iteration, which we substep separately using a constant temperature and ionization rate whenever any of the updated abundances does not converge to 10^{-4} in 20 iterations. We substep the outermost iteration whenever the photon number density in at least one radiation transport cell does not converge to 10% within 10 iterations. Following convergence of the outermost loop, we proceed to its next substep and repeat until all fields have been advanced through the timestep. After updating the ionization, temperature, and radiation fields, we compute the number of new “star particles” and “wind particles” that are spawned. Finally, we update the Eddington tensor field.

Introducing additional physics into GADGET-2 requires us to slow down the calculation in order to achieve a consistent solution. We limit each particle’s individual timestep based on the evolution of its electron abundance as follows:

$$\Delta t \leq \begin{cases} 0.1n_e(dn_e/dt)^{-1} & n_e/n_H > 0.05 \\ 0.05n_H(dn_e/dt)^{-1} & n_e/n_H \leq 0.05 \end{cases} \quad (10)$$

Here, n_e and n_H represent the electron and hydrogen number densities, respectively. This criterion evolves partially-ionized regions cautiously while limiting the ability of neutral regions to slow down the calculation. Note that our fully-implicit solution to Equations 7–9 obliges us to evolve the entire simulation volume’s radiation field whenever any particle’s ionization state is updated. We also limit the global timestep to be no larger than $\Delta \ln(a) = 0.0035$, where a is the cosmological expansion factor.

In Finlator et al. (2009a), we demonstrated that our radiation transport solver reproduces the analytic solution for the growth of ionized regions in expanding media, indicating that it conserves photons and accounts accurately for cosmological terms. We have verified that merging our solver into GADGET-2 preserves this agreement. In addition, we have tested our merged code’s ability to follow the growth of multiple HII regions in a realistic cosmological density field using Test 4 from the cosmological radiative transfer code comparison project (Iliev et al. 2006b). We show that it yields reasonable agreement with results from other codes in the Appendix.

2.3. Identifying Galaxies and Haloes

We isolate the galaxies that have formed within our volume at each redshift using SKID⁴. We infer

⁴ <http://www-hpcc.astro.washington.edu/tools/skid.html>

name	L ¹	winds	RT grid	$M_{h,\min}^2/M_\odot$	time ³	γ/H^4
r6nWnRT	6	no	—	1.4×10^8	1.2	—
r6nWwRT16	6	no	16^3	1.4×10^8	2.1	3.9
r6wWnRT	6	yes	—	1.4×10^8	2.3	—
r6wWwRT16	6	yes	16^3	1.4×10^8	22	5.1
r6nWwRT32	6	no	32^3	1.4×10^8	4.3	3.6
r6wWwRT32	6	yes	32^3	1.4×10^8	31	4.9
r3wWwRT32	3	yes	32^3	1.8×10^7	8.8	5.3
r3nWnRT	3	no	—	1.8×10^7	1.5	—
r6nWHM01	6	no	—	1.4×10^8	1.7	—

TABLE 1. Our simulations. All runs use 2×256^3 particles. The first four simulations explore the relative impact of outflows and radiative feedback. The next four test our sensitivity to resolution effects. The last run assumes the optically-thin EUVB of HM01.

¹ in comoving $h^{-1}\text{Mpc}$

² virial mass of a halo with 100 dark matter and SPH particles.

³ computation time to $z = 6$ in 1000 CPU hours

⁴ ionizing photons emitted per H atom at $x_{\text{H I,V}} = 0.01$

the age and metallicity of each galaxy’s stellar population from the age and metallicity distributions of its star particles. We compute each star particle’s contribution to the galaxy’s integrated stellar continuum by interpolating to its metallicity and age within the Bruzual & Charlot (2003) models, and we account for dust using the Calzetti et al. (2000) model with a normalization that is tied to the stellar metallicity (Finlator et al. 2006).

We identify dark matter halos following the method of Okamoto et al. (2008). First, we identify overdense regions using FOF⁵ with a linking length tied to the (redshift-dependent) virial overdensity. Next, we iteratively compute the center of mass and remove the most distant dark matter particle until only two particles remain. We then grow a sphere around the midpoint between these particles until the enclosed density falls to the virial overdensity. Finally, we define the halo’s baryon mass fraction, SFR, and ionizing luminosity using the particles that fall within this radius.

2.4. Simulations

Table 1 summarizes our simulation suite. The bulk of our discussion will refer to a fiducial cubical volume $6h^{-1}\text{Mpc}$ to a side, which we simulate both with/without momentum-driven outflows and with/without a self-consistently evolved EUVB. We adopt a cosmology in which $\Omega_M = 0.28$, $\Omega_\Lambda = 0.72$, $\Omega_b = 0.046$, $h = 0.7$, $\sigma_8 = 0.82$, and the index of the primordial power spectrum $n = 0.96$. We generate the initial conditions using an Eisenstein & Hu (1999) power spectrum at redshifts of $z = 249$ and 319 for simulations subtending cubical volumes of side length 6 and $3h^{-1}\text{Mpc}$, respectively. We smooth gravitational forces using Plummer equivalent comoving softening lengths of 469 and $234h^{-1}$ parsecs, respectively. The radiative transport simulations have been run using Eulerian grids of 16^3 and 32^3 radiative transport cells. We also ran simulations with eight times the mass resolution and one eighth the volume of our fiducial $6h^{-1}\text{Mpc}$ simulations in order to check numerical convergence. Finally, we have re-run our fiducial

⁵ <http://www-hpcc.astro.washington.edu/tools/fof.html>

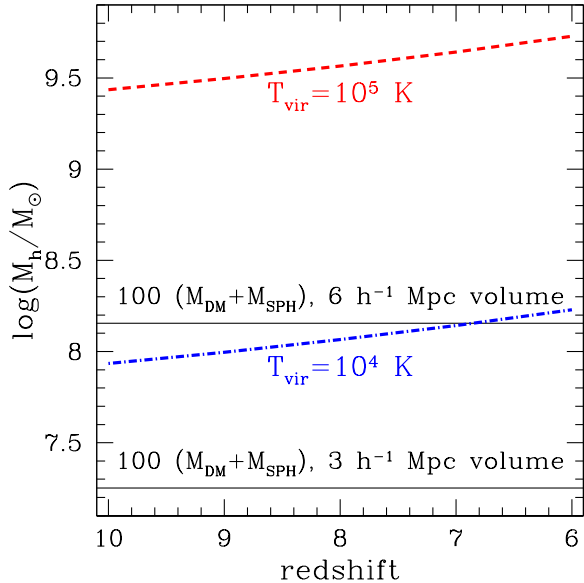


FIG. 2.— The conversion from virial temperature to halo mass as a function of redshift, computed following Barkana & Loeb (1999) with our simulation’s cosmology and a mean molecular weight of $\mu/m_p = 0.59$. The upper and lower solid horizontal lines indicate the masses of halos containing 100 dark matter and gas particles in our 6 and 3 h^{-1} Mpc simulations, respectively; these represent the threshold for halos to possess resolved masses and density profiles (Trenti et al. 2010). Our fiducial (6 h^{-1} Mpc) volume resolves the HI cooling limit for all $z \leq 7$.

simulation without outflows and under the assumption of the optically-thin HM01 EUVB for comparison with previous work.

The sixth column of Table 1 indicates that our RT solver is fairly efficient. The ratio of the number of sources to the number of RT grid cells at $z = 6$ is 774/4016 in the r6wWwRT16 and 1526/32768 in the r6wWwRT32 simulation. Despite this relatively large number of sources, self-consistent RT does not increase the total computation time by more than a factor of four in the absence of outflows (compare the r6nWnRT and r6nWwRT32 simulations). This is because our ionization/RT iteration (the top bubble in the right column of Figure 1) solves the moments of the RT equation for a fixed Eddington tensor. Computing the angular dependence of the ionizing background (that is, updating the Eddington tensors) is computationally expensive, but we do this for only a fraction of RT cells at each timestep.

In the presence of outflows, self-consistent RT increases the computation time by a total factor of 10–15 because outflows generate a significant reservoir of dense gas that lives within one optical depth of the nearest source. Its brief recombination time increases the IGM’s volume-averaged recombination rate while forcing the simulation to evolve on a shorter timestep. Consequently, outflows boost both the computation time and the number of ionizing photons absorbed per hydrogen atom at overlap (seventh column in Table 1).

The goal of the present work is to use a three-dimensional numerical model to study the impact of galactic outflows and photoheating on star formation within photosensitive and photoresistant halos. For reference, we show how this mass range varies with redshift in Figure 2. The black, solid lines indicate the masses of

halos that contain 100 dark matter and gas particles in our fiducial and high-resolution simulations; halos more massive than these thresholds possess converged mass, virial radius, and density profiles (Trenti et al. 2010). By design, our 6 h^{-1} Mpc simulations resolve halos with virial temperatures above 10^4 K at $z \leq 7$. The mass resolution limit of our 3 h^{-1} Mpc volume includes all star formation in atomically-cooling halos at all redshifts, although its small volume limits the number of massive halos that are represented.

3. OUTFLOWS AND PHOTOHEATING I: THEORETICAL INSIGHT

In this Section, we explore how outflows and photoheating impact star formation. We begin by analyzing the baryon mass fraction and SFR as a function of halo mass near the overlap epoch. We will find that photoheating primarily impacts halos below $3 \times 10^9 M_\odot$, above which outflows are the dominant feedback process. We will show that outflows and photoheating couple nonlinearly at all halo masses, although the sign of the effect varies with mass. Next, we weight by halo abundance in order to determine how different halos contribute to the volume-averaged SFRD and ionizing emissivity. We will show that photosensitive halos contribute significantly to the SFRD and the ionizing emissivity through the end of the reionization epoch. Finally, we study how feedback impacts the evolving SFRD.

3.1. The Halos

3.1.1. Baryon Fractions and Star Formation Rates

In Figure 3, we show how the mass fraction in baryons f_{bar} varies with halo mass for each of our simulations at two representative redshifts as indicated. The solid red curves confirm that all halos retain their baryons in the absence of feedback. Allowing a self-consistent EUVB to form (heavy red dotted) suppresses the baryon fraction, with strong suppression visible up to an order of magnitude above the HI cooling limit once the universe is reionized. The slow growth of f_{bar} with mass owes to the hierarchical tendency for halos near the HI cooling limit to accrete much of their mass in the form of halos that are below the limit. Simulations that treat outflows but not an EUVB (heavy blue short-dashed) show that outflows suppress baryon fractions only in halos where star formation is efficient, hence they are negligible at the HI cooling limit. This is an important difference between outflows and an EUVB: photoheating primarily impacts systems near the HI cooling limit while outflows preferentially impact more massive systems owing to hierarchical merging. The separate effects of outflows and photoheating match at roughly $10^9 M_\odot$, above which photoheating weakens while outflows remain efficient by design. Finally, treating both outflows and an EUVB suppresses the baryon fraction at all sampled masses. Curiously, adding galactic outflows to a simulation that already grows an EUVB (that is, going from the dotted red to the dot-dashed blue curves) *boosts* the baryon fraction below $10^9 M_\odot$. We will return to this “suppression of suppression” below.

In order to compare our predictions to previous work, we show with a magenta long-dashed curve the baryon fraction that results without winds and with the optically thin HM01 EUVB. Comparing this with the dotted

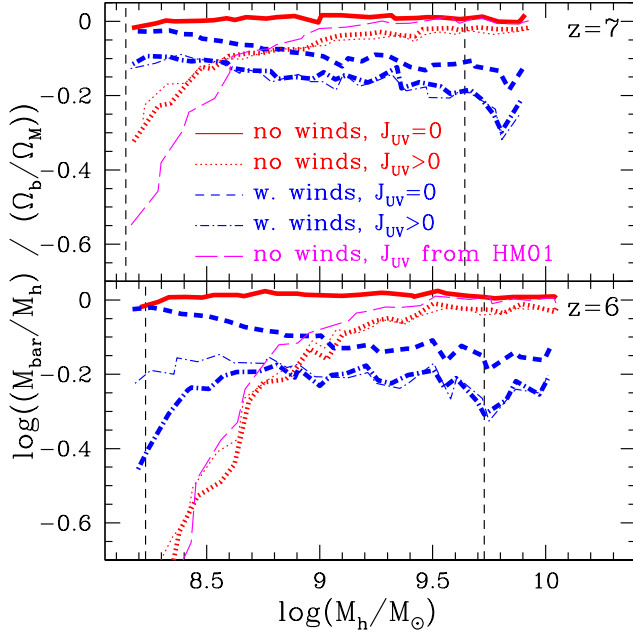


FIG. 3.— The median mass fraction in baryons (f_{bar}) normalized to Ω_b/Ω_M as a function of halo mass. Red and blue curves indicate fiducial simulations with/without outflows and with/without a self-consistent EUVB as indicated. Thick and thin curves indicate that the EUVB is discretized using 16^3 and 32^3 RT cells, respectively. Magenta long-dashed curves denote simulations without outflows and with an optically-thin HM01 EUVB. Left and right vertical dashed lines mark $T_{\text{vir}} = 10^4\text{K}$ and 10^5K from Figure 2. Without feedback, halos contain their global baryon fraction. An EUVB suppresses the baryon fraction in halos below $3 \times 10^9 M_\odot$, with all baryons removed from halos a few times more massive than the HI cooling limit. Including both feedback processes causes the baryon fraction trend to flatten at $0.6\Omega_b/\Omega_M$ for halos above $10^9 M_\odot$.

red curves shows that a spatially-resolved EUVB yields higher baryon fractions at low masses at $z = 7$. Low mass halos have only just been exposed to the EUVB in this simulation because it completes overlap around $z = 7$ (Figure 12), hence their baryon reservoirs have not yet responded. This illustrates the sensitivity of the predicted baryon fractions to inhomogeneous reionization scenarios as compared to models that assume a homogenous EUVB. By $z = 6$, the resulting baryon fractions are within 10% of each other even though the amplitude of the HM01 EUVB is an order of magnitude weaker (Figure 12). This confirms that baryon mass fractions depend weakly on the EUVB amplitude, as opposed to its bias and hardness. This can be understood as follows: A halo’s baryon mass fraction depends mostly on its virial temperature relative to the temperature of the surrounding IGM. The IGM temperature depends mostly on the EUVB hardness at the moment it was reionized because it decouples from the EUVB afterwards. Therefore, boosting the EUVB amplitude in an ionized region does not impact the local baryon fractions because it does not impact the IGM temperature (see also Mesinger & Dijkstra 2008).

In Figure 4, we show how SFR varies with halo mass in the same simulations. In all cases, star formation is negligible in halos below the HI cooling limit because minihalos cannot cool by collisionally exciting neutral hydrogen. Above this cutoff, SFRs rise superlinearly

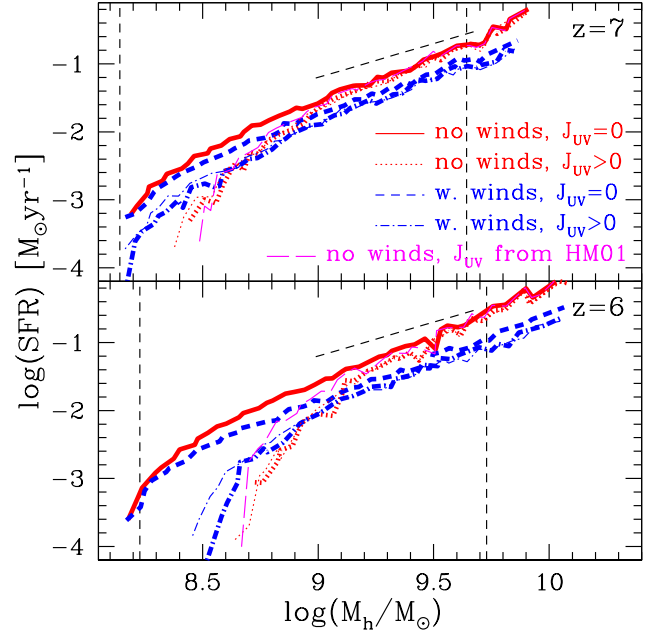


FIG. 4.— SFR as a function of halo mass. Simulations and line styles are as in Figure 3. Star formation is suppressed in halos that approach the HI cooling limit (left vertical dashed line) even though these halos accrete their cosmic complement of baryons. At higher masses, the relation between SFR and halo mass approaches $\text{SFR} \propto M_h$. Overall, halos that are baryon-depleted also show suppressed star formation rates as expected.

over roughly a decade in mass before asymptotically approaching a high-mass trend that is generically steeper than $\text{SFR} \propto M_h$ (black long-dashed line segment with arbitrary normalization). An EUVB raises the cutoff mass roughly a factor of 3 above the HI cooling limit by suppressing the baryon fractions in photosensitive halos (Figure 3). Star formation in halos more massive than $3 \times 10^9 M_\odot$ is weakly affected by the EUVB. Assuming an optically-thin HM01 EUVB and neglecting outflows results in SFRs that are $\sim 10\%$ higher than predictions from our self-consistent EUVB, reflecting slightly higher baryon fractions in the presence of a weaker EUVB (Figure 12). Overall, relative SFRs given different feedback models follow the trends expected from the baryon fractions.

We have fit the simulated trend of SFR versus M_h in the wind models both with and without an EUVB using a fitting function that consists of a power-law at high masses and a turnover at low masses (the turnover uses the functional form of Gnedin 2000):

$$\dot{M}_* = \frac{a \left(\frac{M_h}{10^{10} M_\odot} \right)^b}{\left[1 + (2^{\alpha/3} - 1) \left(\frac{M_h}{M_c} \right)^{-\alpha} \right]^{3/\alpha}} \quad (11)$$

Table 2 gives the parameters of the resulting fits. In obtaining these parameters, we allow the normalization a , high-mass slope b , turnover mass M_c , and turnover slope α to vary independently at each redshift except as indicated in the caption. The normalization a is 10–20% lower in the presence of an EUVB, and it decreases by 40% from $z=10 \rightarrow 6$. The high-mass slope b is always

z	a^1	b	M_c^2	α
r6wWnRT (winds, no EUVB)				
10	0.56	1.29	8.08	3.3
9	0.50 ³	1.29	8.15	3.6
8	0.50	1.35	8.18	5.1
7	0.36	1.29	8.27	4.0
6	0.29	1.30	8.30	5.1
r6wWwRT16 (winds + EUVB)				
10	0.49	1.27	8.10	4.6
9	0.47	1.30	8.18	4.0
8	0.42	1.36	8.22	5.1
7	0.31	1.33	8.36	3.0
6	0.25	1.40	8.61	3.4

TABLE 2. Fits using Equation 11 to the simulated relationship between SFR and M_h in models with outflows, and with and without an EUVB.

¹ in $M_\odot \text{ yr}^{-1}$

² in $\log_{10}(M_c/M_\odot)$

³ Owing to outliers, we were forced to set $a = 0.50 M_\odot \text{ yr}^{-1}$ by hand in this model. All other parameters were allowed to vary freely.

steeper than the linear relation $\text{SFR} \propto M_h$. We have verified that our higher-resolution winds+EUVB model (r3wWwRT32; see Table 1) also yields $b = 1.3\text{--}1.4$, hence this scaling is robust to mass resolution effects. This has implications for the typical size of ionized regions and the expected power spectrum of 21 centimeter fluctuations. For example, Figure 17 of McQuinn et al. (2007) indicates that changing b from 1 to $5/3$ increases the expected power by $\sim 10\times$ at $0.1 h \text{ Mpc}^{-1}$ scales if the neutral fraction is 20%. Our simulations are consistent with the steeper end of this range, indicating more power at large scales. The cutoff mass M_c tracks the HI cooling mass in the absence of an EUVB, but photoheating boosts it by an additional factor of 2 towards $z = 6$. The turnover slope α is not well-constrained because the scatter grows large to low masses, but it lies within the range 3–5. These fits may be compared with other models for galaxy growth during the reionization epoch.

Resolution limitations impact our predictions in two ways. First, the limited spatial resolution of our radiation transport solver can dilute the EUVB as long as ionized regions are not large compared to the grid cells, over-suppressing unbiased halos whose environments would remain neutral for longer at higher resolution. We show this in Figure 3 by using heavy and light curves to compare results from our fiducial $6h^{-1}\text{Mpc}$ volume when the RT grid cells span 375 and $187.5 h^{-1}\text{kpc}$, respectively. At both redshifts, the no-wind simulation is insensitive to spatial resolution because it completes reionization at $z = 7$. By contrast, the simulation that includes outflows and an EUVB is just completing reionization at $z = 6$. In this case, halos below $10^9 M_\odot$ retain more baryons at higher spatial resolution because their (relatively unbiased) environments reionize later. The impact on the predicted SFRs is as expected in Figure 4.

The second resolution limitation involves the limited mass and spatial resolution of our hydrodynamics solver. Our fiducial simulation misses some star formation at redshifts $z > 7$ because the HI cooling mass falls below its 100-particle resolution limit, which delays reionization. For similar reasons, gas clumping is not resolved at densities above the limit given by the SPH smooth-

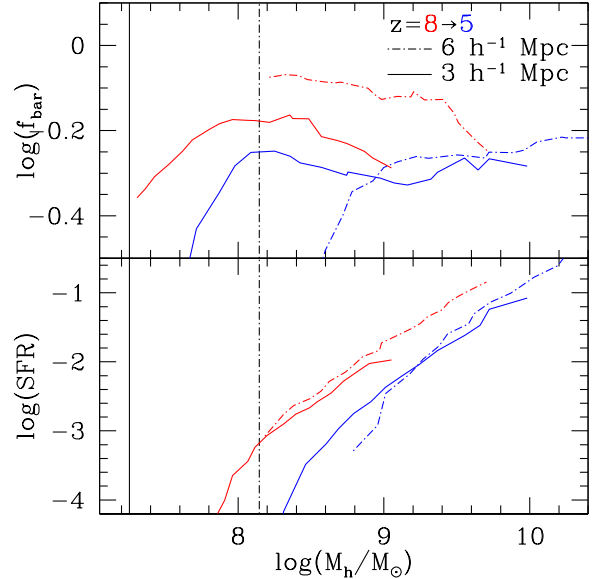


FIG. 5.— (top) The impact of mass resolution on f_{bar} at $z = 8$ (upper red) and $z = 5$ (lower blue). Dot-dashed and solid curves refer to our r6wWwRT16 and r3wWwRT32 simulations, respectively (see Table 1), while the vertical line segments indicate the 100-particle mass resolution limits. (bottom) The impact of resolution limitations on SFR. The units of the y-axes are as in Figures 3–4. We have smoothed all curves with a tophat of width 0.2–0.3 magnitudes. Increasing mass resolution by a factor of 8 suppresses f_{bar} and SFR by a factor of less than $\lesssim 50\%$.

ing length, which delays star formation in all halos. We evaluate these limitations using the r3wWwRT32 simulation, which trades decreased volume for increased mass resolution. Note that this comparison gives an incomplete accounting of resolution limitations because shrinking the cosmological volume delays the growth of structure owing to the lack of long-wavelength density fluctuations (Barkana & Loeb 2004) while increasing the mass resolution accelerates the growth of stellar mass owing to the predominance of small structures at early times (Springel & Hernquist 2003); these effects can partially cancel. A more complete accounting will require increased dynamic range, which is a goal for future work.

In the top panel of Figure 5, we show how f_{bar} evolves during $z = 8 \rightarrow 5$ in our fiducial (r6wWwRT16, dot-dashed) and high-resolution (r3wWwRT32, solid) simulations. At $z = 8$ (upper red curves), increasing the mass resolution by a factor of eight reduces the baryon fractions by 0.1 dex. That this occurs even though the IGM is still essentially neutral in both simulations (Figure 12) indicates that the dominant effect is the ability of simulations with higher mass resolution to resolve star formation and drive outflows sooner, drawing down their baryon reservoirs. By $z = 5$, when both simulations have completed reionization and the fiducial simulation has been forming stars for longer, the predicted baryon fractions at $10^9 M_\odot$ agree well. Below $10^9 M_\odot$, the high-resolution simulation predicts higher baryon fraction because its small volume leads to a delayed overlap epoch (Barkana & Loeb 2004); in essence, halos at the HI cooling mass have only just seen an EUVB in the high-resolution simulation whereas they have seen one for many dynamical times in the fiducial volume.

In the bottom panel of Figure 5, we show that the off-

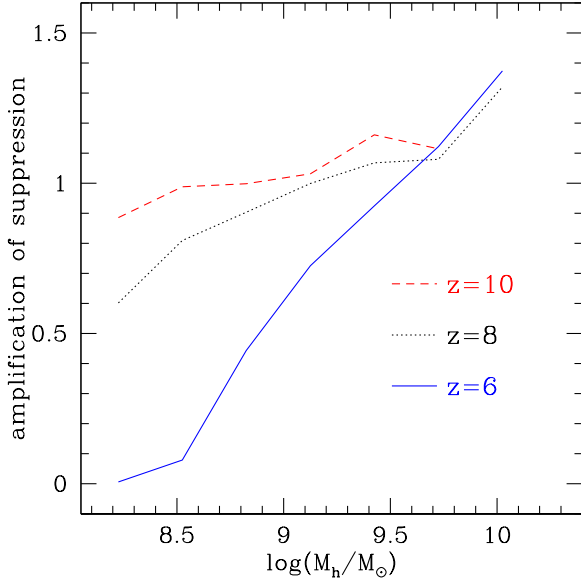


FIG. 6.— Nonlinear amplification of SFR suppression as a function of halo mass in our fiducial volume at three different redshifts as indicated. Suppression of the EUVB by outflows weakens suppression of star formation in photosensitive halos. Coupling between outflowing material and an EUVB boosts the suppression of star formation in photoresistant halos.

sets in f_{bar} translate into offset SFRs as expected: At $z = 8$, the high-resolution simulation has a slightly suppressed SFR while at $z = 5$ its extrapolation to high masses roughly agrees with the trend in the fiducial volume. Halos less massive than $10^9 M_\odot$ have significantly higher SFRs in the high-resolution simulation because their baryon reservoirs have not yet responded fully to reionization. In both cases, the SFR vanishes near the HI cooling mass.

Overall, resolution limitations in our fiducial simulation volume lead to errors of order 0.1 dex in f_{bar} and SFR, particularly in halos less massive than $10^9 M_\odot$. The important point is that they do not change the qualitative evolutionary trends. We conclude that our fiducial simulation volume contains enough dynamic range to capture the relative impacts of different feedback effects even though absolute predictions will have to await the arrival of simulations that sample a larger dynamic range.

3.1.2. Nonlinear Coupling of Feedback Mechanisms by Halo Mass

Comparing the blue dot-dashed and red dotted curves in Figures 3–4 reveals that accounting for both outflows and photoheating leads to higher baryon fractions and SFRs below $\sim 10^9 M_\odot$ than in EUVB-only models. This suppression of suppression has two causes. First, outflows suppress the EUVB (Figure 12), leading to a cooler IGM with a lower Jeans length that permits lower-mass halos to retain their baryons. Second, the simulation is just completing reionization at $z = 6$, hence many of the lowest-mass halos have only recently been exposed to an EUVB and have already cooled their baryon reservoirs to high densities; they will continue to form stars for many dynamical times (Dijkstra et al. 2004a). Both effects weaken the impact of an EUVB on photosensitive

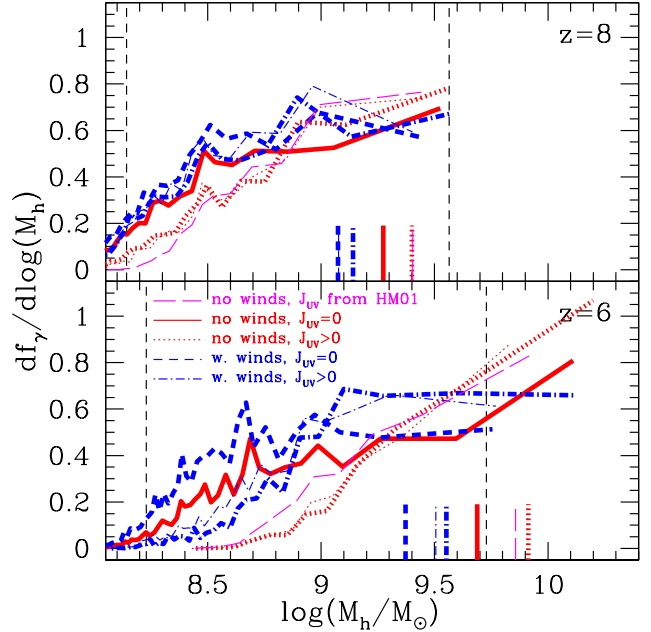


FIG. 7.— The differential fraction of ionizing emissivity as a function of halo mass in each of our models at $z = 8$ (top) and $z = 6$ (bottom). All curves include the effect of low metallicity in low-mass halos, and have been normalized to unit area. Line colors and styles are indicated in the legend. Heavy and light curves distinguish simulations with 16^3 and 32^3 radiation transport cells, respectively. Black vertical dashed lines indicate virial temperatures of 10^4 K (left) and 10^5 K (right). Vertical segments indicate the mass below which 50% of ionizing emissivity occurs. Photosensitive halos contribute significantly in all models, but particularly in the presence of outflows.

halos at the overlap epoch. They are examples of coupling between feedback processes, and they illustrate the role of radiation hydrodynamic simulations in the study of reionization.

We explore feedback coupling further in Figure 6. Here we have computed the “amplification of suppression” in two steps following Pawlik & Schaye (2009): First, we divide the mean trend between SFR and halo mass from runs that include feedback by the trend from the no-feedback run to obtain individual “suppression factors”. Next, we divide the suppression factor from the winds+EUVB model into the product of the suppression factors from the EUVB-only and winds-only models. This yields the factor by which feedback coupling amplifies the total suppression of star formation over what would be expected if outflows and an EUVB interacted linearly. Figure 6 indicates that the sign of feedback amplification depends on halo mass: The tendency of outflows to suppress the EUVB weakens feedback on photosensitive halos, while coupling between outflows and the EUVB amplifies feedback on photoresistant halos. We will return to feedback coupling in § 3.2. We have verified that the amplification factors in Figure 6 are essentially unchanged if we double the spatial resolution of the radiation transport solver.

3.2. Averaging over Cosmological Scales

3.2.1. The Differential Ionizing Emissivity

Figures 3–4 confirm that photoheating suppresses galaxy growth in photosensitive halos. However, they

can still contribute significantly to the volume-averaged SFRD and ionizing emissivity owing to their abundance. We show in Figure 7 the fractional contribution by halos of different masses to the total ionizing emissivity at two representative redshifts. This can be thought of as the integral of the product of the curves in Figure 4 with the dark matter halo mass function, but in practice we simply sum directly over the simulated halos. We weight each halo’s SFR by the (self-consistently predicted) metal mass fraction of its star-forming gas through Equation 2.

In the absence of outflows (red dotted), an EUVB systematically suppresses the total fraction of ionizing photons contributed by lower-mass halos, raising the mass below which 50% of ionizing emissivity occurs (vertical segments) from $10^{9.7}$ to $10^{9.9}M_{\odot}$. The resulting no-outflow EUVB is orders of magnitude stronger than the optically-thin HM01 EUVB (magenta dashed; see also the bottom panel of Figure 12), but it suppresses star formation in low-mass halos only marginally more effectively (as previously seen in § 3.1.1.) Outflows without an EUVB boost the relevance of low-mass halos because hierarchical merging systematically depletes the baryon reservoirs of more massive halos more effectively (Figure 3). In simulations that include both forms of feedback, low-mass halos are more suppressed than in winds-only models owing to photoheating, but less suppressed than in EUVB-only models because the EUVB is weaker.

We use vertical dashed lines to bound the range of halo masses corresponding to $T_{\text{vir}} = 10^{4-5}\text{K}$, or photosensitive halos. Comparing the photosensitive mass range to the vertical segments reveals that photosensitive halos contribute significantly in all models at all epochs, and they generate more than half of all ionizing photons for all $z \geq 6$ in models that include outflows. This fraction is slightly overestimated because our fiducial volume does not sample the halo mass function above $2 \times 10^{10}M_{\odot}$. We can estimate the contribution of more massive halos by weighting the Sheth-Tormen mass function⁶ by the fits in Table 2 and integrating. Correcting for the limitations of our finite volume in this way, we find that photosensitive halos contribute (49,31)% of all star formation at $z = (7, 6)$ in our fiducial winds+EUVB model. This simple estimate neglects the weak dependence of metallicity on halo mass as well as slight inaccuracies at the massive end of the Sheth-Tormen mass function (Lukić et al. 2007). Nevertheless, it confirms that, for realistic inhomogeneous reionization scenarios, the abundance of photosensitive halos more than compensates for their susceptibility to outflows and photoheating.

We have created a galaxy analog to Figure 7 in which the x-axis is the absolute magnitude M_{1600} . Summing over all simulated galaxies, we find that, in our favored winds+EUVB model, half of all ionizing photons originate in galaxies fainter than $M_{1600} \approx -15$. This luminosity is roughly ten times fainter than the deepest current constraints at $z = 6$ (Bouwens et al. 2011b). It lies close to the resolution limit below which star formation is artificially suppressed (Figure 10), hence it is probably biased bright. These considerations reinforce the need for fainter observations to constrain the dominant population of ionizing sources at $z > 6$.

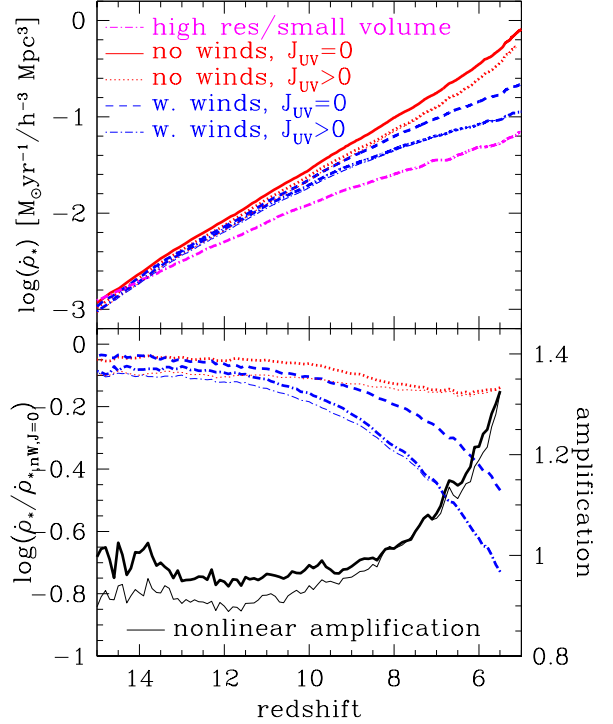


FIG. 8.— (top) The volume-averaged total star formation rate density (SFRD) as a function of redshift. (bottom) The ratio of the curves in the top panel to the curve from the simulation that includes neither outflows nor an EUVB. Line colors and styles are indicated in the legend. Heavy and light curves distinguish simulations with 16^3 and 32^3 radiation transport cells, respectively. Both outflows and an EUVB suppress the SFRD. The solid black curve illustrates feedback amplification. The combined suppression is less than the sum of their separate effects at early times and greater at late times.

3.2.2. The Volume-Averaged Star Formation Rate Density

In Figure 8, we show how the volume-averaged star formation rate density (SFRD) varies with redshift in each of our simulations. The solid red curve in the top panel illustrates how the predicted SFRD grows in simulations without any feedback. Comparing the dotted red and dashed blue curves reveals that outflows and photoheating suppress the SFRD by comparable factors. The dot-dashed blue curve lies significantly below the other curves, indicating that both processes are important in radiation hydrodynamic simulations. Note that the predicted SFRD suppression is expected to be robust to mass resolution at $z \leq 7$ because our simulations resolve the HI cooling limit (Figure 2). At earlier times, they underestimate the impact of photoheating because they only partially account for star formation in halos below $1.4 \times 10^8 M_{\odot}$. Our high-resolution/small-volume simulation has a lower SFRD than the $6h^{-1}\text{Mpc}$ volume following $z = 13$ because it lacks sources brighter than $M_{1600} = -15$ (Figure 10).

We quantify the amount by which feedback suppresses each simulation’s SFRD in the bottom panel. By itself, the EUVB suppresses the SFRD by a factor that grows to $\approx 30\%$ by $z = 6$. Its impact flattens below $z = 7$ because photoresistant halos come to dominate the SFRD. By contrast, the impact of outflows grows with time because the timescale on which galaxies of any

⁶ kindly calculated for us in our assumed cosmology by J. Muñoz

mass replace baryons that they eject grows as the cosmic density declines. Put differently, winds cause the SFR to be dominated by the gas inflow rate at earlier redshifts than in models that ignore outflows. By $z = 6$, outflows reduce the SFRD by $\approx 60\%$. Finally, treating an EUVB and outflows simultaneously suppresses the SFRD by an amount that grows to $\approx 75\%$ by $z = 6$.

In both panels of Figure 8, we use heavy and light curves to compare the results from using coarse and fine grids in our radiation transport solver. The resulting curves appear coincident in the top panel, but the bottom panel clearly shows that lower spatial resolution results in decreased suppression of the SFRD at early times owing to the tendency for coarse grids to dilute the EUVB. The effect is only noticeable while the ionized regions are not large compared to the grid cells, however, and by $z = 8$ it is much smaller than the systematic differences between different models.

Our simulations predict somewhat more suppression by $z = 6$ than Petkova & Springel (2010), who find 0–10% depending on their parameter choice (their Figures 10–11). The difference likely owes predominantly to the fact that the mass resolution of our simulations is $37\times$ as high as in their fiducial volume, a choice that reflects our emphasis on feedback in low-mass halos rather than the IGM. Our high resolution allows us to model the impact of an EUVB on the abundant low-mass halos that fall below their resolution and that dominate star formation at early times (at the expense of subtending a smaller cosmological volume). An additional contribution to the difference may owe to the fact that Petkova & Springel (2010) resolve self-shielding filaments more effectively than in our simulations, which would weaken the suppression of low-mass halos in their calculations.

Figure 8 suggests that the volume-averaged suppression factor from treating outflows and an EUVB simultaneously differs from the sum of their separate impacts. This could occur because an EUVB injects entropy into inflowing gas, increasing its cross section to entrainment by outflows (Kitayama & Yoshida 2005). Alternately, it could occur because outflows “puff up” overdense gas, increasing its cooling time and rendering it more susceptible to photoheating. It is expected given Figure 6, but its overall sign and magnitude depend on the predicted SFR- M_h scaling.

In order to compute the volume-averaged impact of feedback coupling, we multiply the EUVB-only (red dotted) and winds-only (blue dashed) suppression factors to obtain the predicted total suppression factor assuming no feedback amplification (not shown). We then divide this into the true total suppression factor (blue dot-dashed) to find the feedback amplification factor (solid black, right y-axis). Overall amplification is below unity at early times, indicating that the tendency for outflows to suppress the EUVB, thereby boosting star formation in low-mass halos, wins over any more direct coupling between outflows and the EUVB. This was anticipated in Figures 3–4, where we showed that, if the EUVB is grown self-consistently, then photosensitive halos possess higher baryon fractions and SFRs with outflows than without. The effect is stronger if the radiation transport solver uses higher spatial resolution because this further confines the EUVB to the most overdense regions, weakening its impact in voids. Once reionization is well under

way, amplification grows because star formation is increasingly dominated by photoresistant halos. Amplification exceeds 20% by $z = 6$ and continues growing into the post-reionization epoch.

Figures 6 and 8 may be compared with the results of Pawlik & Schaye (2009), who studied feedback coupling using a suite of simulations with/without outflows and with/without an optically-thin EUVB. They found that photoheating and outflows positively amplify each other’s effects at all redshifts. Our study builds on theirs in a number of ways. First, we model an inhomogeneous EUVB, which qualitatively accounts for the possibility that the overdense regions that feed gas into halos could self-shield against the EUVB until relatively late times (Finlator et al. 2009b). In detail, our simulations do not yet completely resolve self-shielding because our RT cells are wider than the length scales of the Lyman Limit systems that host photosensitive halos (~ 10 physical kpc; Schaye 2001). This explains why the baryon fractions in photosensitive halos are not converged in Figure 3. It will be important in future work to model self-shielding within resolution-convergent calculations. Second, we grow the EUVB self-consistently, which accounts for the possibility that outflows suppress the EUVB by suppressing star formation (Figure 12). Finally, we account for metal-line cooling. Metal ions enhance the cooling rate of enriched gas, weakening its response to an EUVB. For the same reason, they boost the SFRD and hence the amplitude of a self-consistent EUVB. Although we do not isolate the impact of metal-line cooling individually, we confirm that it qualitatively preserves feedback coupling.

Quantitatively, our Figure 8 suggests an overall positive amplification of 20% by $z = 6$, as compared to 60% in Figure 1 of Pawlik & Schaye (2009). We attribute the difference primarily to the tendency for outflows to suppress the EUVB, leading to “de-amplification” of suppression in photosensitive halos (Figure 6). Nonetheless, we qualitatively confirm their primary result that hydrodynamic and radiative feedback effects couple nonlinearly. Our predicted amplification would probably converge with theirs at lower redshifts although we have not evolved our simulations past $z = 5$.

4. OUTFLOWS AND PHOTOHEATING II: OBSERVATIONAL IMPLICATIONS

In this section, we study how outflows and photoheating impact the UV continuum LF of galaxies during the reionization epoch. We will show that simulations without outflows overproduce the observed LF while simulations that include outflows are in reasonable agreement. In both cases, an EUVB suppresses the LF normalization by less than 30%. Meanwhile, the LF is not expected to flatten at luminosities brighter than $M_{1600} = -13$, roughly a factor of 100 fainter than current observational limits at $z = 6$.

4.1. Normalization of the Luminosity Function

In Figure 9, we show how outflows and photoheating impact the predicted LF at two representative redshifts. Intuitively, models that predict more strongly suppressed baryon fractions (see Figure 3) also predict more strongly suppressed LFs. The no-feedback model predicts the highest galaxy abundance within the errors. Next is the

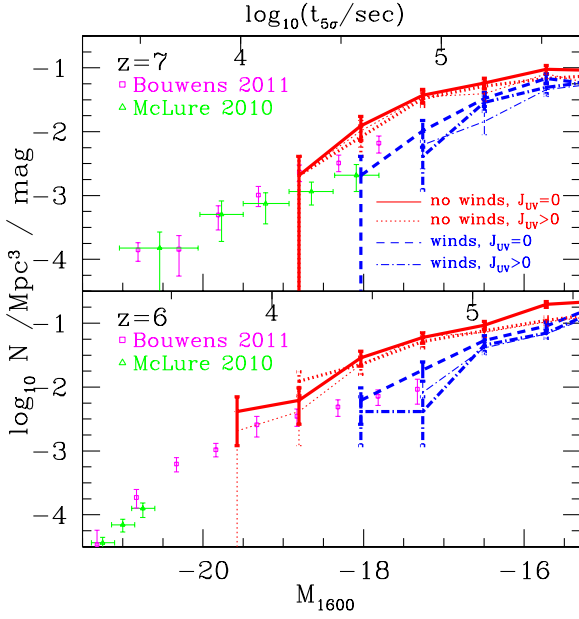


FIG. 9.— The simulated rest-frame ultraviolet continuum LF including dust for simulations with/without outflows and with/without an EUVB at two different redshifts (see the legend for the line styles). We exclude galaxies with fewer than 64 star particles. Simulated errors are Poisson. The top axis indicates the integration time for a 5σ detection in the F200W band of JWST in units $\log_{10}(t/\text{sec})$. Data are from Bouwens et al. (2011b) and McLure et al. (2010). Both outflows and an EUVB suppress the normalization of the LF into improved agreement with observations at $z \leq 7$. Even in the presence of strong feedback, the LF continues to rise steeply below current observational limits.

EUVB-only model, whose LF is suppressed by ≤ 0.2 dex at all sampled luminosities. The third curve corresponds to the wind-only model, whose LF is suppressed by a factor of ≈ 2 at all luminosities. The effect is roughly as strong on bright sources partly because hierarchical growth spreads the impact on smaller objects into larger ones, and partly because we assume that outflows are active at all resolved masses. Finally, including both outflows and an EUVB suppresses the galaxy abundance at all luminosities by a total factor of 2–3.

We also compare these predictions to recent constraints on the reionization-epoch LF (McLure et al. 2010; Bouwens et al. 2011b). At $z = 7$, the simulation including only an EUVB overproduces the observed LF in the regime where the simulated and observed ranges overlap and the simulation’s Poisson errors are not large ($M_{1600} \approx -18$). This confirms previous indications that observations require strong hydrodynamic feedback even at early times (Davé et al. 2006). Including outflows brings the predicted LF into agreement with observations, but now the EUVB’s imprint is weak compared to current observational errors. The observed LF at $z = 7$ has sufficiently large uncertainties that the wind-free simulations are only inconsistent with it at the $1\text{--}3\sigma$ level at any luminosity, but the fact that the offset is systematic argues strongly that it is real. At $z = 6$, the qualitative impact of different feedback effects is the same, but now observations at the faintest luminosities strongly favor models that include outflows. As before, the imprint of a realistic EUVB at observable luminosities is weak compared to uncertainties.

The predicted LFs in Figure 9 are affected by the res-

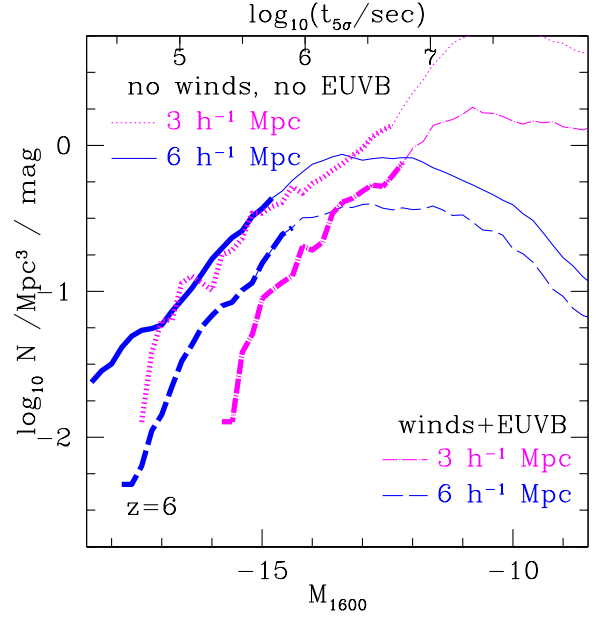


FIG. 10.— The predicted LF at $z = 6$. Upper solid and dotted curves are from our fiducial and high-resolution volumes, respectively, in simulations without any feedback. Lower long-dashed and dot-dashed curves are from simulations of the same volumes that include both outflows and an EUVB. For each simulation, heavy and light curves indicate the predicted LFs brighter and fainter than the luminosity corresponding to our 64 star particle resolution limit, respectively. All curves are smoothed with a boxcar 1 magnitude wide. The top axis indicates the integration time for a 5σ detection in the F200W band of JWST in units $\log_{10}(t/\text{sec})$. Resolution limitations boost the luminosities in the fiducial simulation including feedback (lower long-dashed blue) by a factor of 2–3. The predicted LF rises until at least $M_{1600} = -13$, a factor of 100 fainter than current observational limits at $z = 6$ ($M_{1600} \approx -18$).

olution effects discussed previously. In order to evaluate the strength of these effects, we compare in Figure 10 the predicted LFs from our fiducial and high-resolution simulations at $z = 6$. Light and heavy curves show the LFs obtained from the complete simulated galaxy catalogs and when we exclude simulated galaxies with fewer than 64 star particles, respectively; we have previously argued that this corresponds to the minimum mass for reasonably converged star formation histories (Finlator et al. 2006).

Comparing the lower blue long-dashed and magenta dot-dashed curves suggests that the high-resolution winds+EUVB simulation yields galaxies that are roughly 1 magnitude fainter at constant number density than the low-resolution simulation with the same physical treatments. In other words, halos at $z = 6$ have 2–3 times less star formation at eight times higher mass resolution. This numerical effect occurs in the presence of momentum-driven winds because higher-resolution simulations resolve star formation in lower-mass halos. Lower-mass halos have stronger outflows, hence the massive halos into which they merge grow systematically baryon-deficient (Figure 3). A qualitatively similar effect would occur even in the absence of feedback (as suggested by §3.9 of Kereš et al. 2009), but momentum-driven outflows amplify it significantly. To demonstrate this, we also show the LFs from simulations that omit feedback (upper curves). In this case, the low- and high-resolution simulations agree in the range where they overlap. We conclude that outflows remain required in order

to close the gap between the simulated and observed LFs at $z = 6$, although increasing our resolution could allow us to decrease the wind normalization σ_0 (§ 2.1).

In summary, both outflows and an EUVB suppress the normalization of the predicted LF without significantly changing its shape for absolute magnitudes brighter than $M_{1600} \leq -15$. Over this range in luminosity, the observed LF favors models that include outflows without constraining the EUVB. Resolution limitations artificially boost luminosities in our fiducial volume when outflows are included because outflows preferentially evacuate baryons from low-mass systems. Correcting for this numerical effect could enable us to decrease σ_0 somewhat, but it would not remove the need for outflows.

4.2. Turnover of the Luminosity Function

The LF must flatten below some faint luminosity owing to the impact of photoheating on photosensitive halos and eventually to the HI cooling limit (Figure 2). Observing this feature would be a major step toward constraining the ionizing emissivity that galaxies contribute to cosmological reionization because current “photon counting” reionization calculations are sensitive to the unknown abundance of faint sources (Chary 2008; Muñoz & Loeb 2011; Bouwens et al. 2011b).

Theoretically, the turnover luminosity depends on the reionization history and the nature and strength of star formation feedback (Barkana & Loeb 2000). Regions that reionize sooner or develop a hotter IGM have a higher turnover luminosity. Kulkarni & Choudhury (2011) considered these effects by combining a semi-analytic model for reionization with a Jeans mass calculation of star formation suppression. They found that the mass below which star formation stops varies between $10^{8-10} M_\odot$ at $z = 8$ depending on the bias, corresponding to an absolute magnitude between -12 and -17. While their results are suggestive, their model had difficulty reproducing the evolving LF. Moreover, it did not treat gas flows or the growth of ionized regions in three dimensions, it did not account for the full temperature history of a halo’s environment, and it assumed the timescales over which halos form stars and respond to an EUVB (Dijkstra et al. 2004a) rather than computing them self-consistently. Our numerical simulations are designed to overcome these limitations.

Observationally, the turnover luminosity at $z = 6$ is constrained to be fainter than $M_{UV} = -18$ (Bouwens et al. 2010b). Muñoz & Loeb (2011) have used a semi-analytic model to map this to a minimum star-forming halo mass of $10^{9.4^{+0.3}_{-0.9}} M_\odot$. This is over an order of magnitude more massive than the HI cooling limit (Figure 2). Assuming that some star formation continues down to the HI cooling limit, the LF should continue to rise to lower luminosities.

Figure 9 shows that the predicted LF does not turn over in any model for luminosities brighter than $M_{1600} = -16$. This constitutes a robust prediction that the observed LF will continue to climb to at least this luminosity at $z = 6$ (see also Jaacks et al. 2011). In order to trace the predicted LF to even fainter limits, we refer to the high-resolution simulation including both outflows and an EUVB in Figure 10. This simulation predicts that the LF continues its steep rise to at least $M_{1600} = -13$.

While the light curve flattens at fainter luminosities, the LF at luminosities fainter than -13 is dominated by galaxies with fewer than 64 star particles, hence the flattening likely owes largely to resolution limitations.

Figures 3–4 confirm that an EUVB suppresses photo-sensitive halos, but Figure 10 indicates that even our high-resolution simulation does not fully resolve star-forming galaxies at the turnover luminosity. Nonetheless, we may bound the luminosity range within which a turnover is expected as follows: The turnover must occur in the luminosity range corresponding to $T_{\text{vir}} = 10^{4-5}$ K. At $z = 6$, Equation 11 and Table 2 indicate that the extrapolated (that is, suppression-free) SFRs in halos with $T_{\text{vir}} = 10^4$ K and $T_{\text{vir}} = 10^5$ K are 8.3×10^{-4} and $0.10 M_\odot \text{ yr}^{-1}$, respectively. The predicted relationship between M_{1600} and SFR ($M_\odot \text{ yr}^{-1}$) at $z = 6$ is $M_{1600} = (-18.86 \pm 0.09) + (-2.56 \pm 0.06) \log(\text{SFR})$, hence the unsuppressed luminosities would be -11 and -16, respectively. The bright end of this range may be overly conservative given that the LF in our high-resolution simulation rises past -16 (Figure 10). We therefore predict that the turnover at $z = 6$ will occur between -11 and -13. Future work incorporating significantly larger dynamic range will be required in order to resolve the turnover numerically.

We may draw two conclusions from the faint ends in Figures 9–10. First, hierarchical formation smooths the impact of feedback processes on the LF dramatically such that neither outflows nor an EUVB creates a characteristic feature above $M_{1600} = -13$. Instead, hierarchical growth causes any feedback effect that suppresses low-mass halos to suppress the normalization of the entire LF. We have directly verified that this is true at all $z < 10$. Second, we expect the LF to rise with decreasing luminosity until at least $M_{1600} = -13$ even in the presence of strong outflows and a realistic EUVB. Detecting these faint objects at $z = 6$ will require observations that probe a factor of 100 deeper than the deepest observations to date, requiring 1–10 Msec on JWST (top axes).

5. REIONIZATION HISTORIES

The goal of the present work is to explore the relative impact of outflows and a self-consistently modeled EUVB on star formation in photosensitive halos. In the process, we have simulated cosmological reionization. Our simulations are not designed to resolve Lyman Limit systems or to capture the impact of density fluctuations on length scales that are large compared to our simulation volume, hence neither the ionization nor the recombination rates are expected to be numerically convergent. Nevertheless, it is of interest to examine how the resulting reionization histories compare to observational constraints. In this Section, we compare the volume-averaged neutral hydrogen fraction and EUVB amplitude to observational constraints from the Lyman- α forest and the cosmic microwave background.

5.1. Integrated Optical Depth to Electron Scattering

The probability that photons from the cosmic microwave background scatter off of free electrons following recombination is quantified by the integrated optical depth to Thomson scattering, τ_{es} , which is a key observable that reionization models must confront. Reconciling the observed cosmic star formation

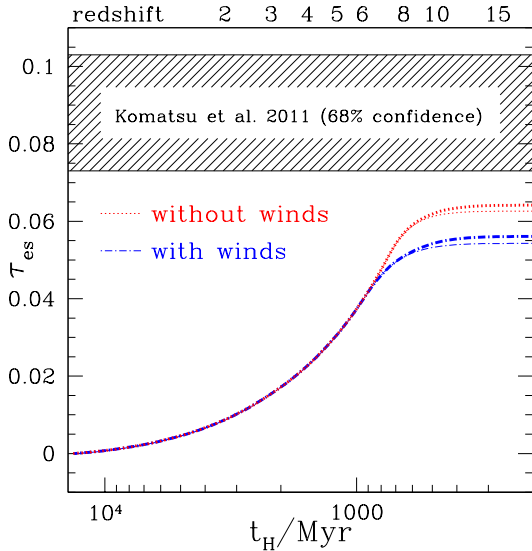


FIG. 11.— The integrated optical depth to electron scattering τ_{es} as a function of the age of the universe. Dotted red and dot-dashed blue curves indicate radiative transfer simulations without and with outflows, respectively. Heavy and light curves compare results from simulations with radiative transfer grids with cell widths of resolution 375 and 187.5 $h^{-1}\text{kpc}$, respectively. All curves include the estimated effect of Helium ionization. Regardless of spatial resolution, helium, and the presence of outflows, simulations underproduce the observed optical depth of Komatsu et al. (2011).

history with τ_{es} is challenging (Robertson et al. 2010; Kulkarni & Choudhury 2011; Haardt & Madau 2011) and depends on a number of assumptions including the evolving abundance of faint galaxies and the IGM recombination rate. It is of interest to ask whether our simulations reproduce τ_{es} because they model these effects self-consistently.

In Figure 11, we show how outflows impact the integrated optical depth to electron scattering τ_{es} as a function of redshift. All curves assume that helium is singly ionized with the same ionization fraction as hydrogen down to $z = 3$, after which it is doubly ionized. Upper red and lower blue curves indicate that simulations without (with) outflows yield $\tau_{es} \approx 0.063(0.054)$, which lies below the observationally-determined 68% confidence range of 0.073–0.103 (Komatsu et al. 2011). Doubling the spatial resolution of our radiation transport solver (light curves) suppresses τ_{es} slightly because simulations with higher resolution treat the small self-shielded regions (such as Lyman-limit systems) that dominate the IGM opacity at late times more accurately (Furlanetto & Oh 2005), which slightly boosts the neutral hydrogen fraction (Figure 12). The difference is small compared to the discrepancy with observations, hence spatial resolution limitations do not dominate the apparent underabundance of free electrons at early times.

Figure 11 may be compared with our post-processing calculations (Finlator et al. 2009b), where we also found values of τ_{es} in the range 0.05–0.07 depending on the choice of ionizing escape fraction. That work yielded higher values for both τ_{es} and the EUVB amplitude while assuming a lower f_{esc} because it did not account for sub-grid recombinations. Our new calculations treat the IGM opacity more correctly, which necessitates a higher f_{esc} and yields a lower τ_{es} and EUVB amplitude.

Petkova & Springel (2010) used a different implemen-

tation of radiation hydrodynamics into GADGET to simulate reionization using 2×256^3 particles within a $10h^{-1}\text{Mpc}$ volume. They accounted for galactic outflows using the model of Springel & Hernquist (2003), hence their simulation is similar to ours, and they found $\tau_{es} = 0.049$ (ignoring helium ionization). When we recompute the τ_{es} from our r6wWwRT32 model omitting helium, we also obtain $\tau_{es} = 0.0493$. The remarkable agreement is probably coincidental given that our simulation considered a smaller volume with higher mass resolution, lower latent heat, a different outflow treatment, and higher f_{esc} . Nevertheless, it remains intriguing that both simulations underproduce τ_{es} . Petkova & Springel (2010) attributed their underestimate partly to the missing contribution of ionized helium and partly to the fact that small cosmological volumes delay the onset of reionization (Barkana & Loeb 2004). We estimate that helium contributes $\Delta\tau_{es} = 0.005$, and our limited volume suppresses τ_{es} by ≈ 0.003 (assuming a redshift delay of 0.035 from Figure 3 of Barkana & Loeb 2004). Summing these effects, we estimate that accounting for both helium and our limited volume would boost the τ_{es} in our fiducial volume to 0.058–0.067, still shy of the observed range. We will discuss other possible explanations for our low τ_{es} below.

5.2. The Neutral Hydrogen Fraction and the Ionizing Background

We show in Figure 12 how the volume-averaged neutral hydrogen fraction and the ionization rate per hydrogen atom vary with redshift and resolution. If outflows are neglected (heavy red dotted), then the volume-averaged neutral hydrogen fraction drops below 0.01 around $z = 7$ while the amplitude of the EUVB at $z = 6$ is overproduced by a factor of 100–1000. Including outflows (heavy blue dot-dashed) delays the completion of reionization to $z = 6$ while bringing both the neutral hydrogen fraction and the EUVB into improved (though imperfect) agreement with observations. Our high-resolution, small-volume simulation (top magenta dot-dashed) does not complete reionization until $z \sim 5$ owing to its high gas clumping and the lack of long-wavelength fluctuations. This history is at odds with the results of Kashikawa et al. (2011, green arrow). These authors found that the Lyman- α LF of LAEs evolves more strongly during $z = 6.5 \rightarrow 5.7$ than the UV continuum LF of LAEs. By assuming that reionization was complete at $z = 5.7$, they used the evolving Lyman- α equivalent width to derive a volume-averaged neutral fraction $x_{\text{H I,V}}$ at $z = 6.5$ of $x_{\text{H I,V}} \leq 0.4$. This suggests that our small volume reionizes too late, although the constraint suffers from uncertainties associated with cosmic variance and the unknown intrinsic Lyman- α LF of LAEs. Our small volume also conflicts with the commonly-accepted reionization redshift $z = 6$ (Fan et al. 2006). Note, however, that constraints from the Lyman- α forest generally assume a spatially-homogeneous EUVB (although see Sbrinovsky & Wyithe 2010). This assumption could lead to biased inferences at early times. McGreer et al. (2011) sidestepped the problem by obtaining an upper limit to $x_{\text{H I,V}}$ from the dark pixel fraction in the Lyman- α forest (cyan arrows). This maximally-conservative measurement yields much higher limits that are in fact consistent with our small volume.

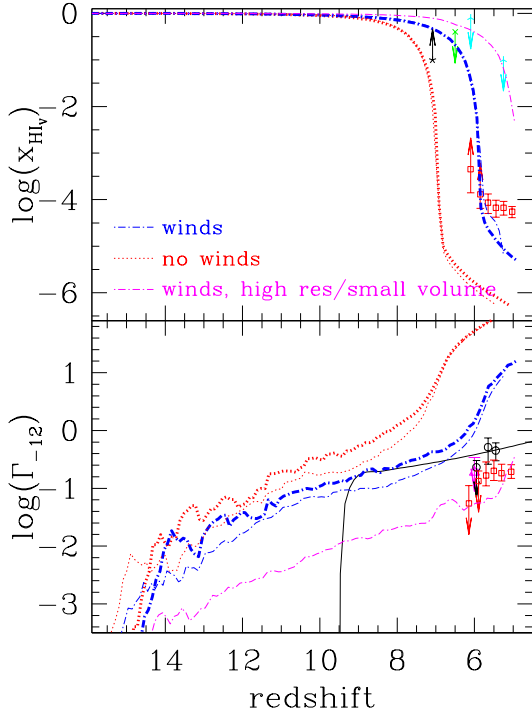


FIG. 12.— (*top*) Volume-averaged neutral hydrogen fraction as a function of redshift. (*bottom*) Ionization rate per hydrogen atom as a function of redshift. Red squares are from Fan et al. (2006), the magenta triangle is from Bolton & Haehnelt (2007), black circles are from Srinovskiy & Wyithe (2010), and the (green, cyan, black) limits with (3, 4, 5)-pointed stars are from Kashikawa et al. (2011), McGreer et al. (2011), and Bolton et al. (2011) respectively. We have updated the McGreer et al. (2011) constraint at $z = 5.25$ to 0.1 (private communication). The simulated curves' colors and styles are as in Figure 11. The solid black curve indicates the observed galaxies+QSOs background HM01. Simulations without outflows readily reionize the Universe by $z = 7$ while dramatically overproducing the observed EUVB. Simulations including outflows complete reionization around $z = 6$ while improving the agreement with the inferred strength of the EUVB. Our high-resolution/small-volume simulation completes reionization at $z = 5$ because it lacks bright sources and resolves more small-scale gas clumping.

However, given that many dark pixels likely correspond to regions that are largely ionized, it remains probable that our small volume requires a higher f_{esc} in order to yield a realistic reionization history.

Our overall reionization histories could be sensitive to the spatial resolution of our radiation transport solver. To explore this, we use heavy and light curves to show reionization histories from simulations that discretize the EUVB using 32^3 and 16^3 grid cells, respectively. Doubling the spatial resolution of our radiation transport solver (light curves) suppresses the EUVB amplitude by a factor of \sim a few at early times without appreciably changing the volume-averaged neutral fraction. We expect its impact on our results to be modest.

It is important to note that, by itself, Figure 12 yields only a joint constraint on the outflow amplitude σ_0 and the ionizing escape fraction f_{esc} because increasing one can be compensated by decreasing the other. Breaking this degeneracy requires galaxy observations, which constrain the outflow amplitude σ_0 . We have previously shown that $\sigma_0 = 150 \text{ km s}^{-1}$ suppresses the predicted galaxy LF into agreement with observations (Davé et al.

2006). Figure 12 shows that combining this assumption with $f_{\text{esc}} = 50\%$ yields a model that simultaneously reproduces observations of galaxies at $z = 6-8$ and the commonly-accepted overlap redshift $z = 6$ (Fan et al. 2006). These considerations illustrate the crucial role of galaxy observations in constraining reionization models.

5.3. Discussion

Figure 11 suggests that the ionized volume fraction is too low at early times while Figure 12 indicates that the ionization rate is too high at late times. At the same time, we have shown that our current wind model yields reasonable agreement with the observed UV continuum LF of galaxies at $z = 6$ (Davé et al. 2006; Finlator et al. 2011; Figure 9), which is proportional to the ionizing emissivity. As a guide for future work toward the goal of devising a self-consistent model for cosmological reionization and feedback effects, it is instructive to consider how our parameter choices could impact our results. The free physical parameters are the latent heat per photoionization ϵ_{HI} , the ionizing escape fraction f_{esc} , and the outflow amplitude σ_0 . The free numerical parameters are the simulation volume and the resolution of our SPH and radiation transport solvers. We now discuss each of these in turn.

Increasing the latent heat per photoionization ϵ_{HI} heats the IGM and boosts Jeans smoothing. This simultaneously suppresses the IGM recombination rate (and through it the neutral hydrogen fraction) while only modestly suppressing the predicted galaxy LF (and through it the amplitude of the EUVB). For example, Petkova & Springel (2010) show that increasing ϵ_{HI} from 6.4 \rightarrow 30 eV accelerates reionization by $\Delta z \approx 0.5$ while roughly doubling the EUVB amplitude. Our current choice $\epsilon_{\text{HI}} = 0.3 \text{ Ryd}$ is motivated directly by the metallicity-dependent stellar continua that our simulations predict. The good agreement that similar simulations have achieved with the observed history of high-redshift star formation (Davé et al. 2006; Finlator et al. 2011) and the metal abundance in galaxies (Finlator & Davé 2008; Davé et al. 2011b) and in the IGM (Oppenheimer & Davé 2006) argues that our predicted stellar continua are realistic. Increasing ϵ_{HI} would therefore run against insight from existing observations. Moreover, it could lead to implausible IGM temperatures. For example, Petkova & Springel (2010) find that assuming a latent heat per photoionization of 30 eV (compared to our 4.08 eV) yields photoionized regions with temperatures in excess of 10^6 K , which may be difficult to reconcile with the tight observed association between cool gas and Lyman-Break galaxies (Weiner et al. 2009; Steidel et al. 2010). It would also violate agreement with the observed distribution of CIV line widths, which does not show evidence for such significant heating (Oppenheimer & Davé 2006). Nevertheless, a modest increase in ϵ_{HI} could improve agreement without violating existing constraints. Such an increase could be associated with spectral filtering through interstellar media.

Increasing f_{esc} causes reionization to occur sooner by strengthening the EUVB (Finlator et al. 2009b). This means that increasing f_{esc} would boost τ_{es} into better agreement with observations of the cosmic microwave background (Figure 11), but at the cost of exacerbat-

ing the disagreement with IGM observations at $z \sim 6$ (Figure 12). Decreasing f_{esc} in the case of the no-wind model would delay reionization, weaken the EUVB, and increase the neutral fraction. This would improve its agreement with observations in Figure 12, but at the expense of further suppressing τ_{es} . The only way in which f_{esc} could simultaneously improve the discrepancies in Figures 11–12 would involve a mass dependence such that f_{esc} is larger in low-mass systems whose star formation halts by $z = 6$ (similar to Iliev et al. 2007).

Weakening outflows (by decreasing σ_0) accelerates reionization in two ways. First, it increases the SFR. As can be seen by examining our no-wind simulation—which corresponds to the extreme case $\sigma_0 = 0$ —this boosts the ionizing emissivity. A weaker effect comes from the fact that weakening outflows at constant f_{esc} decreases the amount of absorbing gas in the IGM. This can be seen by comparing the number of ionizing photons per hydrogen at overlap, the last column in Table 1: No-wind simulations require ≈ 4 photons per hydrogen to reionize whereas wind models require ≈ 5 . Intuitively, outflows relocate absorbing gas from the ISM into the halo so that removing outflows at constant f_{esc} is equivalent to boosting f_{esc} . Both effects boost the EUVB amplitude and τ_{es} . Unfortunately, the EUVB is already too strong, and weakening outflows also causes simulations to overproduce the observed LF of galaxies (Davé et al. 2006), which is now well-constrained. In fact, our most recent simulations suggest that this parameter is more likely too low (too little suppression) than too high (Finlator et al. 2011). Hence it is not likely that boosting τ_{es} by decreasing σ_0 would lead to overall improved agreement.

Increasing the simulation volume at constant mass resolution causes reionization to begin sooner by more completely sampling the rare high- σ peaks that were the first to collapse (Barkana & Loeb 2004). This boosts τ_{es} without affecting the galaxy LF or the IGM temperature at late times. We estimate that this could increase τ_{es} by 0.003–0.004, which helps but may not be enough to bring predictions and observations into agreement.

Increasing the mass resolution would help in two ways. First, it would boost the IGM recombination rate by resolving small self-shielded systems, limiting the mean free path to ionizing photons at late times (Iliev et al. 2005; Aubert & Teyssier 2010). The potential for improvement can be seen by comparing the light blue and magenta dot-dashed curves in the bottom panel of Figure 12. These two simulations adopt the same physical treatments, but the higher-resolution simulation’s (magenta) increased mass and spatial resolution significantly decrease the mean free path to ionizing photons while its small volume lacks the sources that dominate star formation following $z = 13$ (Figure 8). The net result is that the EUVB amplitude is lower even before its SFRD is underproduced while the completion of overlap is delayed until $z = 5$.

The second benefit of increased mass resolution would result from higher ionizing emissivity at early times. To see this, note that Figures 11–12 imply a need for extra ionizations at early times but not later on. This could be achieved through a population of low-mass halos that are active at early times but suppressed by a mature EUVB (Iliev et al. 2007). Our fiducial simulations account completely for star formation in halos above the

HI cooling limit at $z = 7$ of $2 \times 10^8 M_\odot$, but they fail to account for the star formation that must have occurred in lower-mass halos at earlier times, when the HI cooling limit was lower (Figure 2). Increasing our mass resolution would boost star formation prior to $z = 7$ while leaving it unchanged at later times, thus increasing τ_{es} without affecting the EUVB at $z = 6$. Unfortunately, for the reasons mentioned previously, increasing our mass resolution would simultaneously increase the ionizing emissivity and the recombination rate, hence the net effect on τ_{es} requires numerical modeling.

We may estimate how much increasing our dynamic range would increase τ_{es} by taking the larger of the electron abundances predicted by our $3h^{-1}\text{Mpc}$ and $6h^{-1}\text{Mpc}$ simulations at each redshift:

$$\Delta\tau_{\text{es}} = c\sigma_T \int (\max(n_{e,\text{lr}}, n_{e,\text{hr}}) - n_{e,\text{lr}}) dt \quad (12)$$

Here, $n_{e,\text{lr}}$ and $n_{e,\text{hr}}$ represent the electron abundances in the large, low-resolution and small, high-resolution simulations, respectively. Carrying out the integral, we find that $\Delta\tau_{\text{es}} = 7 \times 10^{-6}$, with all of the excess scattering occurring during the redshift range $z = 15\text{--}22$ since the smaller volume has a lower SFRD at later times (Figure 8). This correction is small compared to the discrepancy with Komatsu et al. (2011). In detail, it is underestimated owing to the decreased presence of long-wavelength density fluctuations in our smaller comparison volume. While a full accounting requires simulations with increased dynamic range, we conclude for the present that increased mass resolution would significantly improve the predicted EUVB amplitude and IGM ionization fraction without completely correcting the low τ_{es} .

The final way in which we could reconcile our models with observations involves invoking an additional population of ionizing sources that is active at early times such as Population III stars or miniquasars (Madau et al. 2004). In order for miniquasars to bring τ_{es} into agreement with observations, they must provide an extra $\Delta\tau_{\text{es}} = 0.019$. This could be achieved through a constant ionized fraction of 0.15 from $z = 20 \rightarrow 10$. Maintaining this ionized fraction against recombinations would require 2.4×10^{-19} ionizations $\text{cm}^{-3}\text{s}^{-1}$ (proper units) for a clumping factor of 10, which is a characteristic value from our simulations at an ionized volume fraction of 10%. The ionizing luminosity of Eddington-limited accretion by a black hole of mass M_{BH} is $\sim 10^{51}(f_{\text{esc}}/1)(M_{\text{BH}}/1000M_\odot) \text{ s}^{-1}$ (Madau et al. 2004; Dijkstra 2006), hence this level of ionization could be supported by a population of $1000M_\odot$ black holes with a comoving space density of $\sim 1\text{--}2 \text{ Mpc}^{-3}$. This corresponds roughly to the space density of dark matter halos more massive than $5 \times 10^8 M_\odot$ at $z = 6$, hence such a population could be hosted entirely by atomically-cooled halos.

In summary, Figures 11–12 indicate that our new simulations underproduce the ionization rate at early times while overproducing it at late times. Increasing ϵ_{HI} , the comoving volume, or the mass resolution would yield simultaneous improvement in both respects. However, self-consistency argues against significantly higher values of ϵ_{HI} ; simple estimates indicate that the impact of our

limited volume is small; and a high-resolution simulation suggests that increasing the mass resolution boosts the IGM recombination rate enough to counter the boosted ionizing emissivity at early times. Meanwhile, increasing f_{esc} or decreasing σ_0 would improve τ_{es} while degrading agreement with observations of galaxies and the IGM at $z = 6$. We conclude that simultaneously matching observations of galaxies, the IGM, and the cosmic microwave background may require us to modify assumptions regarding feedback, the nature of the ionizing sources, or the ionizing escape fraction. We plan to consider these possibilities in future work. The important point for our present purposes is that our simulations yield sufficiently realistic reionization histories that we may use them to gain qualitative insight into how outflows and photoheating modulated galaxy growth during the reionization epoch.

6. SUMMARY

We have used a suite of cosmological radiation hydrodynamic simulations to study the impact of galactic outflows and photoheating by a self-consistent, spatially-inhomogeneous EUVB on star formation during the reionization epoch. The major improvements of our work over previous radiation hydrodynamic studies (for example, Gnedin 2000; Petkova & Springel 2010) are that our model includes a treatment for galactic outflows that has previously been tested extensively against observations of galaxies and the IGM from $z = 0 \rightarrow 7$ (§ 1), and that it essentially resolves the HI cooling limit at all relevant redshifts. It is the first study to demonstrate agreement with the observed UV continuum LF, achieve reionization by $z = 6$, and resolve the majority of the star formation that occurs in photosensitive halos. Our major results are as follows:

- By $z = 6$, a self-consistent, inhomogeneous EUVB significantly suppresses the baryon reservoirs and SFRs in halos less massive than $3 \times 10^9 M_\odot$. Meanwhile, the star formation activity in halos more massive than $3 \times 10^9 M_\odot$, which host currently observable galaxies, is essentially unaffected. This suggests that an EUVB acting alone cannot suppress the UV LF into agreement with observations at $z = 6$.
- Momentum-driven outflows can suppress the EUVB and the LF into improved agreement with observations without preventing Population I–II star formation from reionizing the Universe by $z = 6$ as long as we assume that, on average, 50% of ionizing photons escape from the low-mass galaxies that drive reionization.
- Even in the presence of strong outflows, an inhomogeneous EUVB allows photosensitive halos to contribute up to $\sim 50\%$ of all ionizing photons throughout the reionization epoch.
- For halos in the mass range $M_h = 10^{8.2-10.2} M_\odot$, SFR scales as $M_h^{1.3-1.4}$. If the escape fraction is constant, this implies substantially more power in 21-centimeter fluctuations on large scales (0.1 h Mpc^{-1}) than would be expected if $\text{SFR} \propto M_h^{1.0}$.

- High-resolution simulations indicate that the LF continues to rise steeply until at least $M_{1600} = -13$. This implies that reionization was dominated by an abundant population of faint galaxies that has not yet been observed.
- Outflows and an EUVB couple nonlinearly in two ways: First, outflows weaken the EUVB, boosting star formation in photosensitive halos and leading to overall de-amplification of suppression at early times. Second, they amplify the impact of a given EUVB on photoresistant halos as suggested by Pawlik & Schaye (2009), leading to overall amplified suppression of the cosmic comoving SFRD near the end of reionization. By $z = 6$, overall suppression of star formation is 20% greater than would be expected from the two effects acting separately.
- Simulations that achieve reionization at $z = 6-7$ (that is, our fiducial volume) generically underpredict the optical depth to Thomson scattering while slightly overproducing the inferred amplitude of the EUVB and the volume-averaged ionized hydrogen fraction at $z = 6$.
- Discrepancies between observations and models could be alleviated through adjustments to physical or numerical parameters. In general, however, our physical parameters are either indirectly constrained observationally or could only improve agreement significantly with one observable at the expense of another. Simple estimates suggest that improved dynamic range would not boost the predicted τ_{es} into agreement with observations although it would help.
- Observations thus suggest the need for an additional physical scaling that preferentially boosts the ionizing emissivity at early times such as a mass-dependent ionizing escape fraction. Alternatively, an additional population of ionizing sources such as miniquasars could have provided the extra ionizations.

While our results represent a significant step forward in the modeling of reionization-epoch star formation, our predictions are not yet completely converged with respect to mass, spatial, or spectral resolution. The need for higher mass resolution can be seen in our predicted UV luminosity function, which is slightly high owing to the delayed onset of star formation at finite mass resolution (Figure 10). We have also argued that improving our mass resolution would alleviate tensions with inferences from the cosmic microwave background (§5.3).

The need for improved spatial resolution within our radiation transport solver can likewise be seen in two ways. First, comparing the number of photons required to achieve reionization in our r6wWwRT16 and r6wWwRT32 simulations (Table 1, column 6) reveals that the higher-resolution simulation “consumes” 4% fewer photons. This is because the low-resolution simulation smooths over regions that are in reality self-shielded, thereby overestimating gas clumping. Second, the fact

that the light and heavy blue dot-dashed curves in Figures 3–4 are not coincident in the photosensitive range shows that our simulations do not completely resolve the self-shielded regions that host photosensitive halos. A convergent prediction would require RT cell widths that are smaller than the length scales of Lyman Limit systems (~ 10 physical kpc; Schaye 2001), which is four times smaller than the RT cells in our r6wWwRT32 simulation. Current computational resources already allow us to augment our dynamic range somewhat. This will improve our estimate of the IGM recombination rate, confine the EUVB more completely to overdense regions at early times, and resolve the earliest stages of star formation in photosensitive halos.

Another potentially important effect involves fluctuations in the ionizing background on still smaller scales. For example, the interstellar radiation field within an individual galaxy can dominate the EUVB in wavelengths to which its ISM is optically thin (Gnedin 2010; Cantalupo 2010), but our current simulations do not treat it separately from the EUVB. Consequently, they may overestimate the amount of feedback that is required in the form of outflows in order to reproduce the observed LF. This process would also assist in alleviating lingering tensions between the predicted and observed gas fractions of low-mass galaxies, which remain too low at low redshifts in models similar to this one (Davé et al. 2011a). We will consider in future work whether this effect can be incorporated into our subresolution treatment for star formation.

Upgrades to our radiation transport solver allowing multifrequency calculations and the addition of a background from quasars will result in a more accurately-modeled EUVB. Accounting for the longer mean free path of higher-energy photons would raise the IGM temperature in ionized as well as neutral regions (Abel & Haehnelt 1999; Ilić et al. 2006b; Tittley & Meiksin 2007), modifying the relative roles of photosensitive and photoresistant halos.

Finally, recent observations suggest that the way in which dense gas collapses into stars could include dependencies such as the gas metallicity (Gnedin & Kravtsov 2010; Krumholz & Dekel 2011) and the stellar mass density (Shi et al. 2011). Incorporating these dependencies could modify the predicted SFR- M_h relation by delaying star formation activity in photosensitive halos, which would again boost the expected power spectrum of 21 centimeter fluctuations at large scales.

The authors thank Steven Furlanetto, Chael Kruij, Joey Muñoz, Peng Oh, and Moire Prescott for helpful discussions. We thank Volker Springel for making GADGET-2 public. We thank John Wise and Ilian Ilić for sharing their test results with us. We thank the referee for many thoughtful suggestions that improved the draft. Our simulations were run on the University of Arizona’s Xeon cluster. Support for this work was provided by the NASA Astrophysics Theory Program through grant NNG06GH98G, as well as through grant number HST-AR-10647 from the SPACE TELESCOPE SCIENCE INSTITUTE, which is operated by AURA, Inc. under NASA contract NAS5-26555. Support for this work, part of the Spitzer Space Telescope Theoretical Research Program, was also provided by NASA through a contract issued by the Jet Propulsion Laboratory, California Institute of Technology under a contract with NASA. This work was also supported by the National Science Foundation under grant numbers AST-0847667 and AST-0907998. Computing resources were obtained through grant number DMS-0619881 from the National Science Foundation. KF acknowledges support from NASA through Hubble Fellowship grant HF-51254.01 awarded by the Space Telescope Science Institute, which is operated by the Association of Universities for Research in Astronomy, Inc., for NASA, under contract NAS 5-26555.

REFERENCES

- Abel, T., & Haehnelt, M. G. 1999, *ApJ*, 520, L13
Aubert, D., & Teyssier, R. 2010, *ApJ*, 724, 244
Barkana, R., & Loeb, A. 1999, *ApJ*, 523, 54
Barkana, R., & Loeb, A. 2000, *ApJ*, 539, 20
Barkana, R., & Loeb, A. 2001, *Phys. Rep.*, 349, 125
Barkana, R., & Loeb, A. 2004, *ApJ*, 609, 474
Bolton, J. S., & Haehnelt, M. G. 2007, *MNRAS*, 382, 325
Bolton, J. S., Haehnelt, M. G., Warren, S. J., Hewett, P. C., Mortlock, D. J., Venemans, B. P., McMahon, R. G., & Simpson, C. 2011, *MNRAS*, L291
Bouwens, R. J., et al. 2010, *ApJ*, 708, L69
Bouwens, R. J., et al. 2010, *arXiv:1006.4360*
Bouwens, R. J., et al. 2011, *Nature*, 469, 504
Bouwens, R. J., et al. 2011, *arXiv:1105.2038*
Bruzual, G. & Charlot, S. 2003, *MNRAS*, 344, 1000
Bullock, J. S., Kravtsov, A. V., & Weinberg, D. H. 2000, *ApJ*, 539, 517
Calzetti, D., Armus, L., Bohlin, R. C., Kinney, A. L., Koornneef, J., & Storchi-Bergmann, T. 2000, *ApJ*, 533, 682
Cantalupo, S. 2010, *MNRAS*, 403, L16
Chabrier, G. 2003, *PASP*, 115, 763
Chary, R.-R. 2008, *ApJ*, 680, 32
Choudhury, T. R., & Ferrara, A. 2007, *MNRAS*, 380, L6
Davé, R., Finlator, K., & Oppenheimer, B. D. 2006, *MNRAS*, 370, 273
Davé, R., Oppenheimer, B. D., & Finlator, K. 2011, *MNRAS*, 415, 11
Davé, R., Finlator, K., & Oppenheimer, B. D. 2011, *MNRAS*, 1158
Dekel, A., & Silk, J. 1986, *ApJ*, 303, 39
Dijkstra, M., Haiman, Z., Rees, M. J., & Weinberg, D. H. 2004, *ApJ*, 601, 666
Dijkstra, M., Haiman, Z., & Loeb, A. 2004, *ApJ*, 613, 646
Dijkstra, M. 2006, *New Astronomy Reviews*, 50, 204
Dunlop, J. S., McLure, R. J., Robertson, B. E., Ellis, R. S., Stark, D. P., Cirasuolo, M., & de Ravel, L. 2011, *arXiv:1102.5005*
Eisenstein, D. J., & Hu, W. 1999, *ApJ*, 511, 5
Fan, X., et al. 2006, *AJ*, 132, 117
Furlanetto, S. R., & Oh, S. P. 2005, *MNRAS*, 363, 1031
Furlanetto, S. R., Oh, S. P., & Briggs, F. H. 2006, *Phys. Rep.*, 433, 181
Furlanetto, S. R., & Oh, S. P. 2009, *ApJ*, 701, 94
Finkelstein, S. L., Papovich, C., Giavalisco, M., Reddy, N. A., Ferguson, H. C., Koekemoer, A. M., & Dickinson, M. 2010, *ApJ*, 719, 1250
Finlator, K., Davé, R., Papovich, C., & Hernquist, L. 2006, *ApJ*, 639, 672
Finlator, K., & Davé, R. 2008, *MNRAS*, 385, 2181
Finlator, K., Özel, F., & Davé, R. 2009, *MNRAS*, 393, 1090
Finlator, K., Özel, F., Davé, R., & Oppenheimer, B. D. 2009, *MNRAS*, 400, 1049
Finlator, K., Oppenheimer, B. D., & Davé, R. 2011, *MNRAS*, 410, 1703

- Gardner, J. P., et al. 2009, *Astrophysics in the Next Decade*, 1
- González, V., Labbé, I., Bouwens, R. J., Illingworth, G., Franx, M., & Kriek, M. 2011, *ApJ*, 735, L34
- Gnedin, N. Y. 2000, *ApJ*, 542, 535
- Gnedin, N. Y., & Fan, X. 2006, *ApJ*, 648, 1
- Gnedin, N. Y. 2010, *ApJ*, 721, L79
- Gnedin, N. Y., & Kravtsov, A. V. 2010, *ApJ*, 714, 287
- Grazian, A., et al. 2011, *A&A*, 532, A33
- Greif, T. H., Johnson, J. L., Bromm, V., & Klessen, R. S. 2007, *ApJ*, 670, 1
- Grogin, N. A., et al. 2011, arXiv:1105.3753
- Haardt, F. & Madau, P. 2001, in *Clusters of Galaxies and the High Redshift Universe Observed in X-rays*, 64 (HM01)
- Haardt, F., & Madau, P. 2011, arXiv:1105.2039
- Haiman, Z. 2009, *Astrophysics in the Next Decade*, 385
- Hu, E. M., Cowie, L. L., Barger, A. J., Capak, P., Kakazu, Y., & Trouille, L. 2010, *ApJ*, 725, 394
- Iliev, I. T., Scannapieco, E., & Shapiro, P. R. 2005, *ApJ*, 624, 491
- Iliev, I. T., Mellema, G., Pen, U.-L., Merz, H., Shapiro, P. R., & Alvarez, M. A. 2006, *MNRAS*, 369, 1625
- Iliev, I. T., et al. 2006, *MNRAS*, 371, 1057
- Iliev, I. T., Mellema, G., Shapiro, P. R., & Pen, U.-L. 2007, *MNRAS*, 376, 534
- Iliev, I. T., Shapiro, P. R., McDonald, P., Mellema, G., & Pen, U.-L. 2008, *MNRAS*, 391, 63
- Jaacks, J., Choi, J.-H., & Nagamine, K. 2011, arXiv:1104.2345
- Kashikawa, N., et al. 2011, *ApJ*, 734, 119
- Katz, N., Weinberg, D. H., & Hernquist, L. 1996, *ApJS*, 105, 19
- Kennicutt, R. C. 1998, *ApJ*, 498, 541
- Kereš, D., Katz, N., Fardal, M., Davé, R., & Weinberg, D. H. 2009, *MNRAS*, 395, 160
- Kitayama, T., & Yoshida, N. 2005, *ApJ*, 630, 675
- Koekemoer, A. M., et al. 2011, arXiv:1105.3754
- Kohler, K., Gnedin, N. Y., & Hamilton, A. J. S. 2007, *ApJ*, 657, 15
- Komatsu, E., et al. 2011, *ApJS*, 192, 18
- Kulkarni, G., & Choudhury, T. R. 2011, *MNRAS*, 412, 2781
- Krumholz, M. R., & Dekel, A. 2011, arXiv:1106.0301
- Lukić, Z., Heitmann, K., Habib, S., Bashinsky, S., & Ricker, P. M. 2007, *ApJ*, 671, 1160
- Madau, P., Haardt, F., & Rees, M. J. 1999, *ApJ*, 514, 648
- Madau, P., Rees, M. J., Volonteri, M., Haardt, F., & Oh, S. P. 2004, *ApJ*, 604, 484
- Malhotra, S., & Rhoads, J. E. 2006, *ApJ*, 647, L95
- McGreer, I. D., Mesinger, A., & Fan, X. 2011, *MNRAS*, 412, 1096
- McKee, C. F. & Ostriker, J. P. 1977, *ApJ*, 218, 148
- McLure, R. J., Dunlop, J. S., Cirasuolo, M., Koekemoer, A. M., Sabbi, E., Stark, D. P., Targett, T. A., & Ellis, R. S. 2010, *MNRAS*, 403, 960
- McLure, R. J., et al. 2011, arXiv:1102.4881
- McQuinn, M., Lidz, A., Zahn, O., Dutta, S., Hernquist, L., & Zaldarriaga, M. 2007, *MNRAS*, 377, 1043
- Mellema, G., Iliev, I. T., Alvarez, M. A., & Shapiro, P. R. 2006, *NewA*, 11, 374
- Mesinger, A., & Dijkstra, M. 2008, *MNRAS*, 390, 1071
- Muñoz, J. A., & Loeb, A. 2011, *ApJ*, 729, 99
- Murray, N., Quataert, E., & Thompson, T. A. 2005, *ApJ*, 618, 569
- Oesch, P. A., et al. 2011, arXiv:1105.2297
- Oh, S. P. 2002, *MNRAS*, 336, 1021
- Okamoto, T., Gao, L., & Theuns, T. 2008, *MNRAS*, 390, 920
- Oppenheimer, B. D., & Davé, R. 2006, *MNRAS*, 373, 1265
- Oppenheimer, B. D., & Davé, R. 2008, *MNRAS*, 387, 577
- Oppenheimer, B. D., Davé, R., & Finlator, K. 2009, *MNRAS*, 396, 729
- Oppenheimer, B. D., Davé, R., Kereš, D., Fardal, M., Katz, N., Kollmeier, J. A., & Weinberg, D. H. 2010, *MNRAS*, 406, 2325
- Ouchi, M., et al. 2010, *ApJ*, 723, 869
- Pawlik, A. H., & Schaye, J. 2011, *MNRAS*, 412, 1943
- Pawlik, A. H., & Schaye, J. 2009, *MNRAS*, 396, L46
- Petkova, M., & Springel, V. 2010, arXiv:1008.4459
- Pieri, M. M., & Martel, H. 2007, *ApJ*, 662, L7
- Rauch, M., Becker, G. D., Haehnelt, M. G., Gauthier, J.-R., Ravindranath, S., & Sargent, W. L. W. 2011, arXiv:1105.4876
- Robertson, B. E., Ellis, R. S., Dunlop, J. S., McLure, R. J., & Stark, D. P. 2010, *Nature*, 468, 49
- Schaerer, D. 2003, *A&A*, 397, 527
- Schaye, J. 2001, *ApJ*, 559, 507
- Schwarz, H. A. 1870, *Vierteljahrsschrift der Naturforschenden Gesellschaft in Zürich*, 15, 272
- Shapiro, P. R., Giroux, M. L., & Babul, A. 1994, *ApJ*, 427, 25
- Shi, Y., Helou, G., Yan, L., Armus, L., Wu, Y., Papovich, C., & Stierwalt, S. 2011, *ApJ*, 733, 87
- Siana, B., et al. 2010, *ApJ*, 723, 241
- Sokasian, A., Abel, T., Hernquist, L., & Springel, V. 2003, *MNRAS*, 344, 607
- Springel, V., & Hernquist, L. 2003, *MNRAS*, 339, 312
- Springel, V. 2005, *MNRAS*, 364, 1105
- Srbnovsky, J. A., & Wyithe, J. S. B. 2010, *Publications of the Astronomical Society of Australia*, 27, 110
- Stark, D. P., Ellis, R. S., Richard, J., Kneib, J.-P., Smith, G. P., & Santos, M. R. 2007, *ApJ*, 663, 10
- Steidel, C. C., Erb, D. K., Shapley, A. E., Pettini, M., Reddy, N., Bogosavljević, M., Rudie, G. C., & Rakic, O. 2010, *ApJ*, 717, 289
- Sutherland, R. S. & Dopita, M. A. 1993, *ApJS*, 88, 253
- Thoul, A. A., & Weinberg, D. H. 1996, *ApJ*, 465, 608
- Tilvi, V., et al. 2010, *ApJ*, 721, 1853
- Tittle, E. R., & Meiksin, A. 2007, *MNRAS*, 380, 1369
- Trac, H., & Cen, R. 2007, *ApJ*, 671, 1
- Trac, H., Cen, R., & Loeb, A. 2008, *ApJ*, 689, L81
- Trac, H., & Gnedin, N. Y. 2009, arXiv:0906.4348
- Treister, E., Schawinski, K., Volonteri, M., Natarajan, P., & Gawiser, E. 2011, *Nature*, 474, 356
- Trenti, M., Smith, B. D., Hallman, E. J., Skillman, S. W., & Shull, J. M. 2010, *ApJ*, 711, 1198
- Weiner, B. J., et al. 2009, *ApJ*, 692, 187
- Willott, C. J., et al. 2010, *AJ*, 139, 906
- Wise, J. H., & Abel, T. 2011, *MNRAS*, 414, 3458
- Wise, J. H., & Abel, T. 2008, *ApJ*, 685, 40
- Wise, J. H., & Abel, T. 2008, *ApJ*, 684, 1
- Wong, W. Y., Moss, A., & Scott, D. 2008, *MNRAS*, 386, 1023
- Zheng, Z., Cen, R., Trac, H., & Miralda-Escudé, J. 2010, *ApJ*, 716, 574

APPENDIX

TEST OF MULTIPLE SOURCES

Test 4 of Iliev et al. (2006b) involves evolving the ionization fronts from 16 sources embedded in a static cosmological density field, hence it tests the code’s ability to resolve the impact of density fluctuations on the shape of the ionization front. It also tests the code’s treatment for photoheating and radiative cooling. For multifrequency techniques it tests spectral filtering, but as our code is currently monochromatic, it illustrates the systematics associated with neglecting the ability of high-energy photons to preheat neutral regions (Iliev et al. 2006b; Tittle & Meiksin 2007).

We represent the density field using a uniform grid of SPH particles whose masses vary in such a way as to reproduce the test requirement in the absence of SPH smoothing. During run-time, our code extracts the gridded densities from the SPH particles using a “clouds-in-cells” approach. This smooths the density field on a length scale of ~ 3 times the mean particle separation. Consequently, the opacity field that our radiation transport solver “sees” does not exactly reflect the test requirement, and we do not expect our results to agree quantitatively with those of other codes. We have verified that increasing the number of SPH particles per grid cell from 1 to 8 yields ionized regions whose shapes agree more closely with reference results. We enclose the test volume in 4 layers of opaque boundary cells that prevent

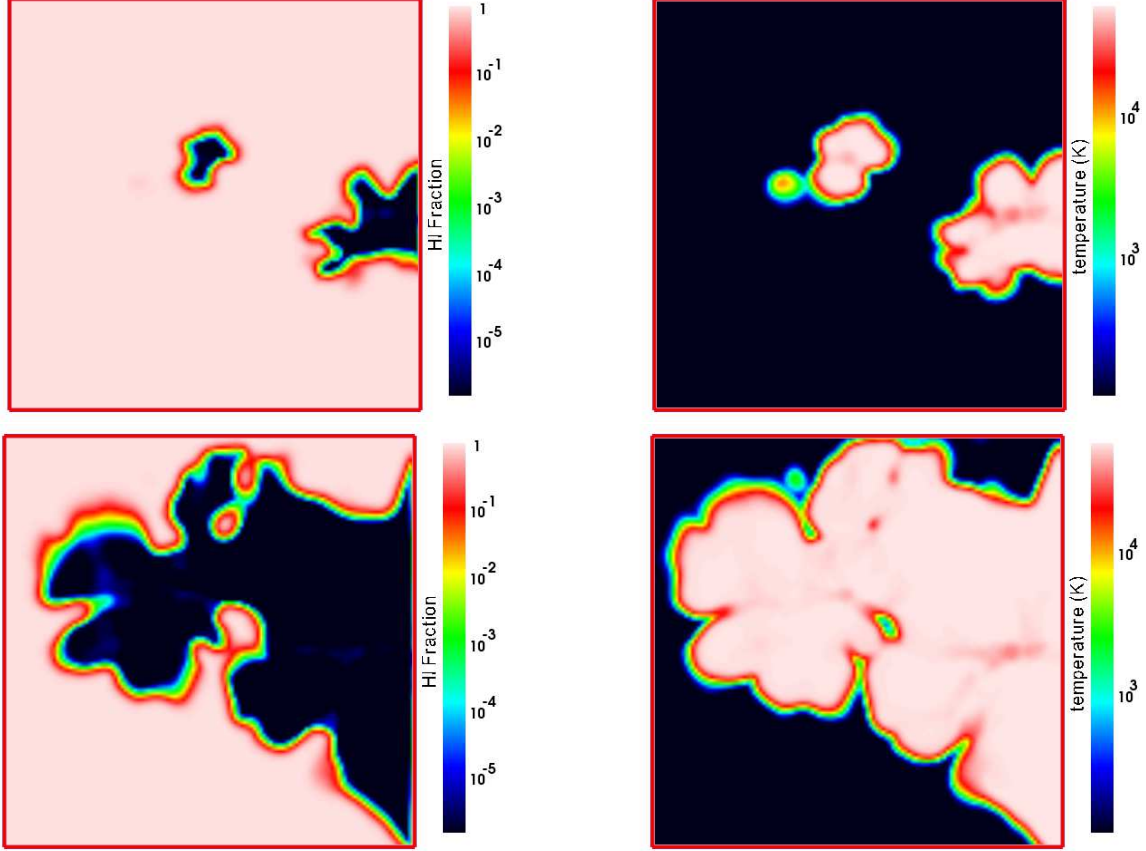


FIG. 13.— Ionization state (*left*) and temperature (*right*) of the Test 4 case at $t = 0.05$ Myr (*top*) and $t = 0.2$ Myr (*bottom*). This test was run with 256^3 SPH particles and 128^3 RT cells. The ionization front is significantly smoother than those produced by other codes (Iliev et al. 2006b; Wise & Abel 2011; Pawlik & Schaye 2011) owing to the diffusive nature of our radiation transport solver, and the IGM behind the ionization front remains cold because our monochromatic solver does not treat spectral hardening. Nonetheless, the volume and temperature of the ionized region are reasonable, indicating that the code accurately evolves the IGM’s thermal and ionization evolution.

photons from “wrapping around” because our code is optimized for periodic boundary conditions. The latent heat per photoionization is 1.177 Ryd, which is appropriate for a $T = 10^5$ K blackbody in the optically-thick approximation. We smooth the Eddington tensor with a 27-cell tophat filter in order to suppress rapid spatial fluctuations in the radiation pressure tensor. This step ensures photon conservation at the cost of rendering the radiation field more diffusive. We have found empirically that smoothing is not required in our current cosmological simulations because their spatial resolution is generically much lower than that of Test 4, preventing the appearance of sharp peaks in the radiation pressure tensor. However, future cosmological simulations at higher spatial resolution may require smoothing. We run the test in an expanding Universe at $z = 8.84922$ with $\Omega_b = \Omega_M = 1$, and we adjust H_0 and the box size so that the proper density and volume match the required test conditions. Strictly speaking, Test 4 is meant to be a test of static density fields and should not be run in an expanding frame. However, its duration of 0.4 Myr is small compared to the Hubble time at this redshift, hence cosmological effects are negligible.

We show maps of the neutral hydrogen fraction and temperature in a slice of the simulation volume in Figure 13. The ionization maps (left column) show similar morphologies to the results from other codes (see, for example, Figure 19 of Wise & Abel 2011 or Figure 10 of Pawlik & Schaye 2011). This broad agreement indicates that our approach accounts reasonably well for fluctuations in the EUVB on length scales that are large compared to individual cells. In detail, our approach yields smoother ionization fronts than ray-tracing codes partly because SPH smooths the density field on scales comparable to the mean particle separation, and partly because the moment method smooths the radiation field on scales comparable to the cell length. While this motivates further work in order to capture fluctuations at length scales that are closer to the size of the RT grid cells, we do not expect it to alter the interaction between galaxies and the EUVB when averaged over cosmological volumes.

For a more quantitative comparison, we show in Figure 14 how the volume-averaged and mass-averaged ionized fractions evolve in our own test (black solid) and in tests conducted using ENZO+MORAY (Wise & Abel 2011) and C²-RAY (Mellema et al. 2006). Two kinds of differences are apparent. First, the predicted reionization topologies differ. The ratio $x_{\text{HII,M}}/x_{\text{HII,V}}$ exceeds unity in all codes at early times, indicating that the initial stages of reionization are robustly “inside-out” (Iliev et al. 2006a). The ray-tracing codes switch to an “outside-in” topology by the time the ionized fraction reaches 60%. This indicates that ionization fronts have arrived in underdense regions and is reminiscent of the “inside-outside-middle” topology discussed in Finlator et al. (2009b). Meanwhile, our moment

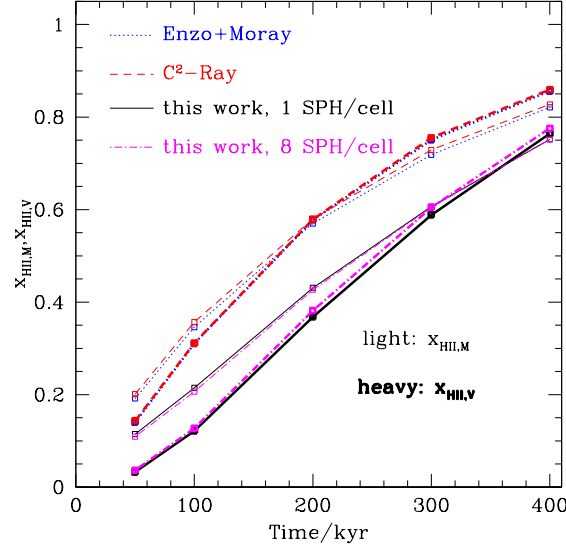


FIG. 14.— Mass-weighted (light) and volume-weighted (heavy) ionized fraction versus time in our approach (solid black) and using C^2 -RAY (dashed red) and ENZO+MORAY (dotted blue). Solid black and dot-dashed magenta curves indicate test runs with 1 and 8 SPH particles per grid cell, respectively. The topology of reionization and the ionized fractions are both sensitive to the density field’s accuracy. Broadly, our predicted ionized fractions are somewhat lower than in the reference codes, indicating that our method predicts a slower reionization history in this test case.

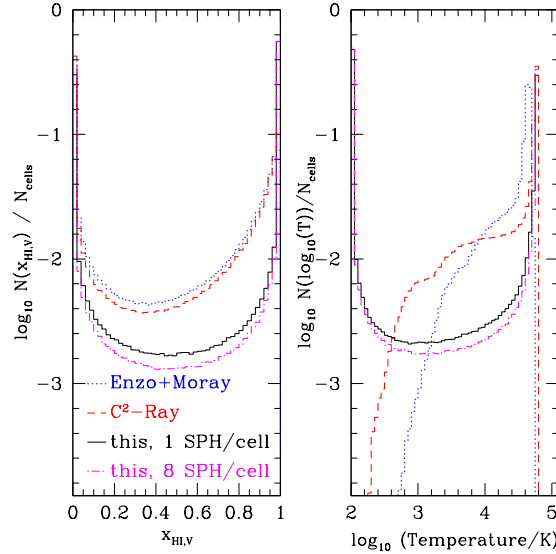


FIG. 15.— Histograms of neutral hydrogen fraction (left) and temperature (right) at 0.2 Myr. Colors and line styles are as in Figure 14. Reionization occurs somewhat more slowly in our code as compared to the other codes, and the absence of high-energy photons leads to a systematically cooler IGM.

approach maintains a purely inside-out topology until the ionized fraction reaches nearly 70%, indicating significantly stronger ionization-front trapping in overdense regions. Increasing the number of SPH particles per grid cell moves the transition to earlier times, suggesting that the difference between the predicted topologies may owe largely to our smoothed density field. The second difference involves the reionization rate. Our method predicts that reionization proceeds more slowly than in the reference codes, with the neutral fractions $\sim 10\%$ higher at the end of the test. Comparing the solid black and dot-dashed magenta curves reveals that increasing the accuracy with which we capture the required density field weakens ionization-front trapping and accelerates reionization. However, the difference is slight, suggesting that increasing our spatial resolution indefinitely would not necessarily bring our results into agreement with the reference runs.

In order to explore our code’s slower reionization rate further, we show histograms of neutral fraction and temperature at 0.2 Myr in Figure 15. The distribution of neutral fractions has a similar shape in all four cases, but our code shows fewer cells in all bins of $x_{\text{HI},V}$ except the neutral bin $x_{\text{HI},V}=0.98-1.0$. In fact, the fraction of cells in which $x_{\text{HI},V}=1$ is $\sim 40\%$ in our test runs and $< 10^{-3}$ in both reference runs. This dominates the difference between our code and

the reference codes in Figure 14. Accounting more completely for partial ionization by high-energy photons in neutral regions would improve agreement. For similar reasons, our code does not pre-heat neutral regions, leading to an enhanced volume fraction at low temperature with respect to the reference codes.

In summary, our radiation hydrodynamic code yields reionization histories that are similar to results from other codes. This implies that our approach accounts reasonably well for fluctuations in the EUVB on scales larger than an individual cell. In detail, however, underdense regions are colder and more neutral in our code than in others. This partly reflects the difficulty of translating a gridded density field into a grid of SPH particles. Mostly, however, it simply reflects the absence of high-energy photons that broaden ionization fronts and preheat neutral regions.